Hydrogen Epoch of Reionization Array (HERA)

David R. DeBoer[1], Aaron R. Parsons[1], James E. Aguirre[2], Paul Alexander[3], Zaki S. Ali[1], Adam P. Beardsley[4], Gianni Bernardi[5,6], Judd D. Bowman[4], Richard F. Bradley[7], Chris L. Carilli[8], Carina Cheng[1], Eloy de Lera Acedo[3], Joshua S. Dillon[1], Aaron Ewall-Wice[9], Gcobisa Fadana[6], Nicolas Fagnoni[3], Randall Fritz[6], Steve R. Furlanetto[10], Brian Glendenning[8], Bradley Greig[11], Jasper Grobbelaar[6], Bryna J. Hazelton[12,13], Jacqueline N. Hewitt[9], Jack Hickish[1], Daniel C. Jacobs[4], Austin Julius[6], MacCalvin Kariseb[6], Saul A. Kohn[2], Telalo Lekalake[6], Adrian Liu[1,16], Anita Loots[6], David MacMahon[1], Lourence Malan[6], Cresshim Malgas[6], Matthys Maree[6], Zachary Martinot[2], Nathan Mathison[6], Eunice Matsetela[6], Andrei Mesinger[11], Miguel F. Morales[12], Abraham R. Neben[9], Nipanjana Patra[1], Samantha Pieterse[6], Jonathan C. Pober[14], Nima Razavi-Ghods[3], Jon Ringuette[12], James Robnett[8], Kathryn Rosie[6], Raddwine Sell[6], Craig Smith[6], Angelo Syce[6], Max Tegmark[9], Nithyanandan Thyagarajan[4], Peter K. G. Williams[15], and Haoxuan Zheng[9]

[1] Department of Astronomy, University of California, Berkeley, CA, USA; ddeboer@berkeley.edu
[2] Department of Physics and Astronomy, University of Pennsylvania, Philadelphia, PA, USA
[3] Cavendish Astrophysics, University of Cambridge, Cambridge, UK
[4] School of Earth and Space Exploration,Arizona State University, Tempe, AZ, USA
[5] Department of Physics and Electronics, Rhodes University, P.O. Box 94, Grahamstown, 6140, South Africa
[6] SKA-SA, Cape Town, South Africa
[7] National Radio Astronomy Observatory, Charlottesville, VA, USA
[8] National Radio Astronomy Observatory, Socorro, NM, USA
[9] Department of Physics, Massachusetts Institute of Technology, Cambridge, MA, USA
[10] Department of Physics and Astronomy, University of California, Los Angeles, CA, USA
[11] Scuola Normale Superiore, Pisa, Italy
[12] Department of Physics, University of Washington, Seattle, WA, USA
[13] eScience Institute, University of Washington, Seattle, WA, USA
[14] Physics Department, Brown University, Providence, RI, USA
[15] Harvard-Smithsonian Center for Astrophysics, Cambridge, MA, USA

Abstract

The Hydrogen Epoch of Reionization Array (HERA) is a staged experiment to measure 21 cm emission from the primordial intergalactic medium (IGM) throughout cosmic reionization ($z = 6$–12), and to explore earlier epochs of our Cosmic Dawn ($z \sim 30$). During these epochs, early stars and black holes heated and ionized the IGM, introducing fluctuations in 21 cm emission. HERA is designed to characterize the evolution of the 21 cm power spectrum to constrain the timing and morphology of reionization, the properties of the first galaxies, the evolution of large-scale structure, and the early sources of heating. The full HERA instrument will be a 350-element interferometer in South Africa consisting of 14 m parabolic dishes observing from 50 to 250 MHz. Currently, 19 dishes have been deployed on site and the next 18 are under construction. HERA has been designated as an SKA Precursor instrument. In this paper, we summarize HERA's scientific context and provide forecasts for its key science results. After reviewing the current state of the art in foreground mitigation, we use the delay-spectrum technique to motivate high-level performance requirements for the HERA instrument. Next, we present the HERA instrument design, along with the subsystem specifications that ensure that HERA meets its performance requirements. Finally, we summarize the schedule and status of the project. We conclude by suggesting that, given the realities of foreground contamination, current-generation 21 cm instruments are approaching their sensitivity limits. HERA is designed to bring both the sensitivity and the precision to deliver its primary science on the basis of proven foreground filtering techniques, while developing new subtraction techniques to unlock new capabilities. The result will be a major step toward realizing the widely recognized scientific potential of 21 cm cosmology.

---

[16] Hubble Fellow.

1. Introduction

The Hydrogen Epoch of Reionization Array (HERA; http://reionization.org) is a staged experiment to use the redshifted 21 cm line of neutral hydrogen to characterize our Cosmic Dawn, from the formation of the first stars and black holes $\sim$0.1 Gyr after the Big Bang ($z \sim 30$) through the full reionization of the intergalactic medium (IGM) $\sim$1 Gyr later ($z \sim 6$). By directly observing the large scale structure of the primordial IGM as it is heated and reionized, HERA complements probes at other wavelengths, adding transformative capabilities for understanding the astrophysics and fundamental cosmology of our early universe. Taking advantage of a new understanding of bright foreground systematics, HERA's purpose-built radio interferometer is optimized to deliver high signal-to-noise measurements of redshifted 21 cm emission to detect and characterize the Epoch of Reionization (EOR).

The power that observations of highly redshifted hydrogen emission have for answering key science about our early universe has motivated a resurgence of interest in low-frequency arrays—most with the primary objective of measuring the EOR. These include the Precision Array Probing the Epoch of Reionization (PAPER; Parsons et al. 2010), the Murchison Widefield Array (MWA; Tingay et al. 2013), the LOw Frequency ARray (LOFAR; van Haarlem et al. 2013), and the Long Wavelength Array (Ellingson et al. 2009), as well as systems for existing dish arrays like the Very Large Array (Kassim et al. 2013) and the Giant Metrewave Radio Telescope (GMRT; Paciga et al. 2011). These experiments all struggle with the inherent challenge of simultaneously meeting stringent sensitivity requirements while suppressing foregrounds $\sim$5–6 orders of magnitude brighter than the 21 cm signal (Bernardi et al. 2009; Pober et al. 2013a; Dillon et al. 2014). HERA improves on its predecessors by bringing significantly more sensitivity to bear on the angular and spectral scales where recent work (discussed in Section 3.2) has indicated that the power spectrum of the EoR may dominate over foregrounds.

The HERA experiment will comprise 350 14 m parabolic dishes (320 in a dense core + 30 outriggers) in the South African Karoo Radio Astronomy Reserve (see Figure 1 for a rendering). HERA's antenna element and its compact configuration are optimized for robust power spectrum detection, delivering the requisite collecting area inexpensively, while carefully controlling foreground systematics. The design and construction of this instrument is supported by the HERA collaboration consisting of the following Partner institutions: Arizona State University (Tempe, AZ, USA), Brown University (Providence, RI, USA), University of California Berkeley (Berkeley, CA, USA), University of California Los Angeles (Los Angeles, CA, USA), University of Cambridge (Cambridge, UK), Massachusetts Institute of Technology (Cambridge, MA, USA), National Radio Astronomy Observatory (Charlottesville, VA, USA), University of Pennsylvania (Philadelphia, PA, USA), Scuola Normale Superiore di Pisa (Pisa, Italy), SKA-South Africa (Cape Town, South Africa), and University of Washington (Seattle, WA, USA). Additional Collaborators are at Harvard University (Cambridge, MA, USA), University of KwaZulu Natal (Durban, South Africa), University of Western Cape (Cape Town, South Africa), Imperial College London (London, UK) and California State Polytechnic University (Pomona, CA, USA). The South African National Research Foundation Square Kilometer Array South Africa (SKA-SA) group is a key partner in HERA's construction and science.

HERA's first stage of development has been funded under the US National Science Foundation's Mid-Scale Innovations Program, which has supported the construction of a 19-element array for testing instrumental performance and manufacturability on location. The first 19-element array is complete and, with additional funding from Cambridge University, construction is now underway on the next 18 elements. The total 37 elements, to be completed in 2016, will provide a factor of about five more sensitivity than PAPER-128 and provide a significant chance at detecting the EoR power spectrum signal. The next proposed phase will build out to 128 elements and use the existing 128 dual-polarization analog and digital signal paths that have been in use with PAPER. HERA-128 should provide a robust detection of the EOR signal and allow some characterization. Finally, extending to 2020, HERA will build out to 350 elements to further EOR science as a function of redshift and spatial scale, potentially producing the first images of the EOR. As a low-frequency science array on an SKA site, HERA has been designated as an SKA Precursor instrument.

This paper is structured as follows. Section 2 gives a high-level overview of the science motivating HERA's construction, including primary and secondary science objectives. Section 3 presents the techniques used to make the measurement. Section 4 presents the high-level requirements and Section 5 presents the system description. Section 6 presents a brief status and outline the deployment timetable and Section 7 concludes by summarizing and providing additional context.

Figure 1. Rendering of the 320-element core (left) of the full HERA-350 array and picture of 19 HERA 14 m, zenith-pointing dishes (with PAPER elements in the background) currently deployed in South Africa (right).
(A color version of this figure is available in the online journal.)

2. Scientific Background

The *Cosmic Dawn* of our universe is one of the last unexplored frontiers in cosmic history. This history is summarized in Figure 2, starting with the Big Bang on the left. The hot, young universe expands and cools slowly in the background while gravitational instability around concentrations of dark matter causes primordial density fluctuations to grow. The Cosmic Dawn represents a specific epoch in this growth, where the first stars and galaxies formed and illuminated the universe en route to forming the astronomical structures we see today. Ultimately, this early population of gravitationally condensed material produced sufficiently energetic flux to reionize the IGM from its previous neutral state in a period called the EOR. This period is shown in Figure 2 as the rapid transition from separated large reionized "bubbles" to the merged reionized state and to structures that begin to resemble the denizens of our current universe. The structure of the IGM thus contains a panoply of information about the underlying astrophysical and cosmological phenomena governing cosmic evolution.

The evolution of the cosmic structure depends on the local and average cosmic density, the relative velocities of baryons and dark matter, and the sizes and clustering of the first galaxies to form. But it also depends on the constituents of those first galaxies—so-called Population III stars (stars formed very early with little to no elements heavier than helium), later generation stars, stellar remnants, X-ray binaries, and early supermassive black holes. Bulk properties like ultraviolet and X-ray luminosities and spectra also affect the thermal and ionization states of the IGM. The wealth of unexplored physics during the Cosmic Dawn, culminating in the EOR, led the most recent US National Academies astronomy decadal survey entitled *New Worlds, New Horizons* to highlight it as one of the top three "priority science objectives" for the decade (National Academy of Science 2010).

Exploring the interplay of galaxies and large-scale structure during the EOR requires complementary observational approaches. Measurements of the Cosmic Microwave Background (CMB; the photons permeating the universe after
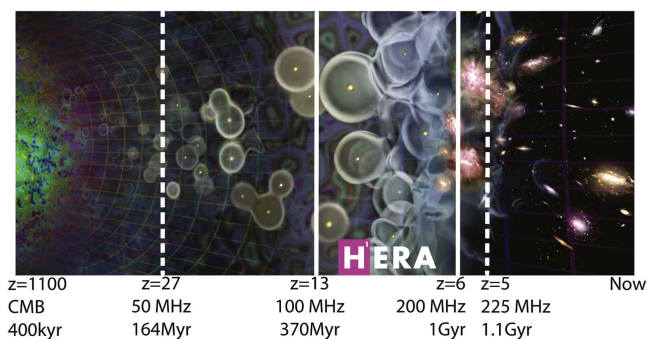

z=1100　　z=27　　　　z=13　　　z=6　z=5　　　　Now
CMB　　　50 MHz　　100 MHz　　200 MHz　225 MHz
400kyr　　164Myr　　370Myr　　1Gyr　1.1Gyr

Figure 2. Rendering of cosmic evolution from just after the Big Bang to today (background image credit Loeb/*Scientific American*). The labels show the redshift and the frequency of the redshifted hydrogen line (rest frequency 1420 MHz) at different ages of the universe. The solid white lines bracket the HERA EOR band and the dashed ones bracket the extended frequency goal. CMB observations observe the afterglow of the Big Bang (far left) and Baryonic Acoustic Oscillation (BAO) surveys proposed target $z \approx 0.8$–2.5. Limited surveys span back to about $z \approx 7$.
(A color version of this figure is available in the online journal.)

becoming transparent to its own radiation by the recombination of the protons and electrons about 400,000 years after the Big Bang) by COBE, *WMAP* and Planck provide initial conditions for structure formation. Thomson scattering of CMB photons by the ionized particles constrains the integrated column of ionized gas and kinetic Sunyaev–Zel'dovich measurements constrain the duration of the "patchy" phase of cosmic structures. But even with these measurements, the detailed evolution of the IGM is only loosely constrained (Haiman & Holder 2003; Mortonson & Hu 2008; Mesinger et al. 2012; Zahn et al. 2012). Lyα absorption features in quasar and γ-ray burst spectra give ionization constraints at the tail end of reionization ($z < 7$, Fan et al. 2006; McGreer et al. 2015), but these features saturate at low neutral fractions $x_{\mathrm{H\,I}} \gtrsim 10^{-4}$, where $x_{\mathrm{H\,I}}$ is the fraction of hydrogen in its neutral state.

Measurements of galaxy populations in deep *Hubble Space Telescope* observations have pinned down the bright end of the
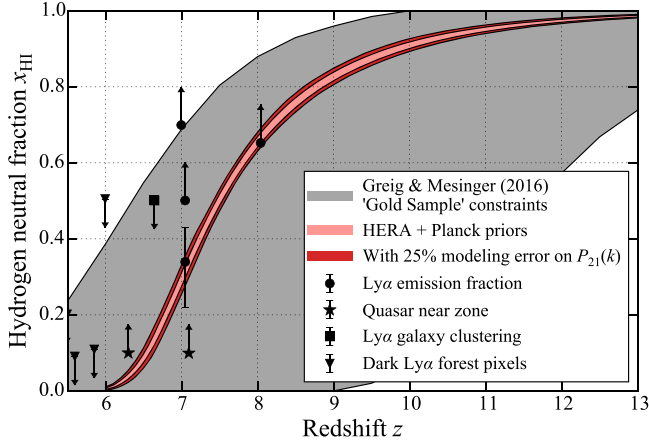
Figure 3. Combining direct constraints on $x_{\rm H\,I}$, the hydrogen neutral fraction, as a function of redshift (black points) with *Planck* priors (Planck Collaboration et al. 2015) yields an inferred 95% confidence region (gray; Greig & Mesinger, in prep.). HERA constraints with (dark red) and without (pale red) a conservative 25% modeling error in the 21 cm power spectrum can dramatically narrow this confidence region (Liu & Parsons 2016). Included for reference are constraints from the fraction of Lyα emitting galaxies (Pentericci et al. 2014; Schenker et al. 2014), quasar near-zone studies (Bolton et al. 2011; Mortlock et al. 2011; Schroeder et al. 2013), Lyα galaxy clustering (McQuinn et al. 2007; Ouchi et al. 2010), and counts of dark Lyα pixels (McGreer et al. 2015).

galaxy luminosity function at $z \lesssim 8$ (Schenker et al. 2013; Bouwens et al. 2015b) and are pushing deeper (e.g., McLeod et al. 2015), but producing a consistent ionization history requires broad extrapolations to lower-mass galaxies and ad hoc assumptions about the escape fraction of ionizing photons and the faint-end cutoff of ionizing galaxies (Bouwens et al. 2015a; Robertson et al. 2015). Similarly, deducing the ionization state of the IGM from quasar proximity zones (Carilli et al. 2010; Bolton et al. 2011; Bosman & Becker 2015) and the demographics of Lyα emitting galaxies (Fontana et al. 2010; Schenker et al. 2012; Treu et al. 2012; Dijkstra et al. 2014) is uncertain and highly model-dependent. See Figure 3 for these constraints on the hydrogen neutral fraction as a function of redshift. As shown, existing probes are limited in their ability to constrain reionization, and will be for the foreseeable future. HERA uses another complementary probe —the 21 cm "spin-flip" transition of neutral hydrogen—to bring new capabilities in this area. The next sub-sections outline these goals.

2.1. Precision Constraints on Reionization

HERA's primary science goal is to transform our understanding of the first stars, galaxies, and black holes, and their role in driving reionization. Through power-spectral measurements of the 21 cm line of hydrogen in the primordial IGM, HERA will be able to direct constrain the topology and evolution of reionization, opening a unique window into the
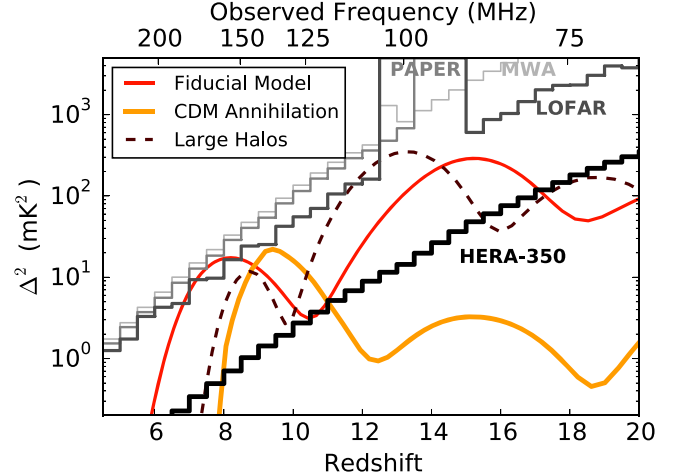

Figure 4. 1σ thermal noise errors on $\Delta^2(k)$, the 21 cm power spectrum, at $k = 0.2\,h\,{\rm Mpc}^{-1}$ (the dominant error at that k) with 1080 hr of integration (black) compared with various heating and reionization models (colored). Sensitivity analysis is per Table 1 and the associated text.

complex astrophysical interplay between the first luminous objects and their environments. The spectral nature of 21 cm cosmology means that the signal at each observing frequency can be associated with an emission time (or distance) to determine both the time evolution and three-dimensional spatial structure of ionization in the IGM. This 3D structure encodes information about the clustering properties of galaxies, allowing us to distinguish between models, even if they predict the same ionized fraction. With a new telescope optimized for 3D power-spectral measurements and with support for theoretical modeling efforts, the HERA program will advance our understanding of early galaxy formation and cosmic reionization.

HERA builds on the advances of first-generation 21 cm EoR experiments led by HERA team members, particularly the Donald C. Backer Precision Array for Probing the Epoch of Reionization (PAPER; Parsons et al. 2010), the MWA (Bowman et al. 2013; Tingay et al. 2013), the MIT EoR experiment (MITEoR; Zheng et al. 2014) and the Experiment to Detect the Global EoR Step (EDGES; Bowman & Rogers 2010). Recent measurements have produced the first astrophysically constraining upper limits on the 21 cm EoR power spectrum, providing evidence for significant heating in the IGM prior to reionization (Parsons et al. 2014, Liu et al 2016; Ali et al. 2015; Pober et al. 2015). However, current experiments cannot expect more than marginal detections of the EoR signal. Figure 4 compares telescope sensitivities as a function of redshift to models of the evolving, spherically averaged 21 cm EoR power spectrum, characterized by the dimensionless power spectrum parameter $\Delta^2(k) \equiv k^3 P(k)/2\pi^2$. The expected performance of HERA relative to current

Table 1
Predicted S/N of 21 cm Experiments for an EoR Model with 50% Ionization at $z = 9.5$, with 1080 hr Observation, Integrated over a Δz of 0.8

Instrument	Collecting Area (m^2)	Foreground Avoidance	Foreground Modeling
PAPER	1,188	0.77σ	3.04σ
MWA	3,584	0.31σ	1.63σ
LOFAR NL Core	35,762	0.38σ	5.36σ
HERA-350	**53,878**	**23.34σ**	**90.97σ**
SKA1 Low Core	416,595	13.4σ	109.90σ

and planned telescopes to detect the peak of reionization (as well as the total collecting area) is shown in Table 1.

These sensitivity calculations done were performed with 21cmSense[17] (Pober et al. 2013b, 2014). Foreground avoidance represents an analysis comparable to Ali et al. (2015), whereas foreground modeling allows significantly more k modes of the cosmological signal to be recovered. For the foreground avoidance approach, several design optimizations allow HERA to achieve significantly higher sensitivities than LOFAR and comparable sensitivities to SKA, despite its modest collecting area. The primary driver is HERA's compact configuration. The 21 cm signal is a diffuse background, with most of its power concentrated on large scales; therefore, most of an instrument's sensitivity to the EOR comes from short baselines. Since HERA is a filled aperture out to ∼300 m, for a fixed collecting area, one fundamentally cannot build an array with more short baselines (without using smaller elements—and HERA's dishes are already significantly smaller than either LOFAR or SKA stations). Within a ∼150 m radius from the center, LOFAR has only 11 stations, amounting to just over 8000 m² of collecting. Within this radius, the SKA is nearly filled, with ∼80% the collecting area of HERA; however, the SKA underperforms in the foreground avoidance schema, where long baselines lose more modes of the power spectrum to foreground contamination (Parsons et al. 2012a).

HERA's 21 cm measurements can be used in conjunction with semi-analytic models to constrain the ionization history. The red band in Figure 3 shows the forecasted 95% confidence region derived from HERA data after marginalizing over astrophysical and cosmological parameters. Figure 5 shows the results of a Markov Chain Monte Carlo (MCMC) pipeline for fitting models to 21 cm power spectrum data (Greig & Mesinger 2015), which we have conservatively limited to the range $8 < z < 10$ (although in practice a much broader bandwidth will be available; see Section 4.2). Based on the excursion-set formalism of Furlanetto et al. (2004) and the 21cmFAST code (Mesinger et al. 2011), this code models the astrophysics of reionization with three free parameters (see Figure 5 for details). While the existing experiment with the
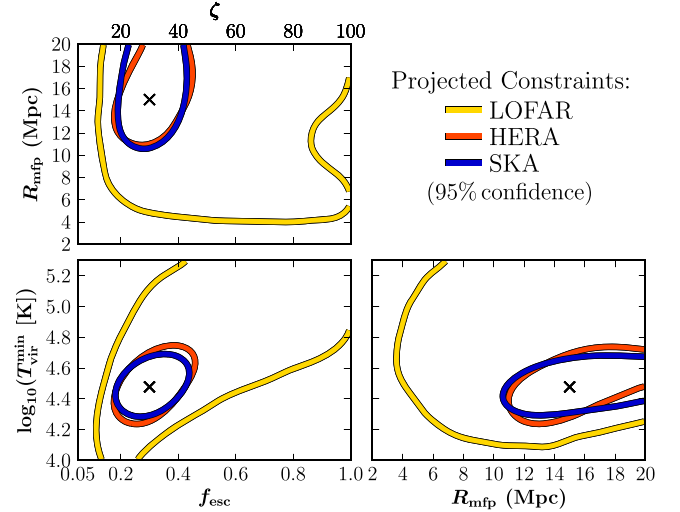
Figure 5. Projected likelihood contours from an MCMC analysis for astrophysical parameters of reionization. Model parameters are $T_{\rm vir}^{\rm min}$ (minimum virial temperature of ionizing galaxies); $R_{\rm mfp}$ (mean free path of ionizing photons in H II regions); and ζ_0 (ionizing efficiency of galaxies). Also shown are constraints on the derived ionizing escape fraction, $f_{\rm esc}$. Adapted from Greig & Mesinger (2015).

most collecting area, the LOFAR (van Haarlem et al. 2013; Yatawatta et al. 2013), provides some ability to constrain these parameters, HERA's constraints are significantly more precise and are comparable to what could be achieved with the SKA. Additionally, HERA's constraints enable principal component parameterizations of the sky-averaged 21 cm signal measurements pursued by experiments such as EDGES, increasing their signal-to-noise and thus their science return (Liu & Parsons 2016).

2.2. Secondary Scientific Objectives

2.2.1. Precision Cosmology

By advancing our understanding of reionization astrophysics, HERA will improve CMB constraints on fundamental cosmological parameters by removing the optical depth τ as a "nuisance" parameter. HERA measurements will be able to break the degeneracy between the constraints on τ and the sum of the neutrino masses $\sum m_\nu$, which has been identified as a potential problem for Stage 4 CMB lensing experiments (Allison et al. 2015; Manzotti et al. 2016). A HERA-informed estimate of τ enables CMB lensing experiments to achieve a 0.012 eV error on $\sum m_\nu$ (Liu et al. 2016). This would represent a ∼5σ cosmological detection of the neutrino masses even under the most pessimistic assumptions still allowed by neutrino oscillation experiments (Allison et al. 2015), making HERA key to understanding neutrino physics. HERA's estimate of τ would also break the degeneracy between τ and the amplitude of matter fluctuations (expressed in Figure 6 as σ_8) that arises when using
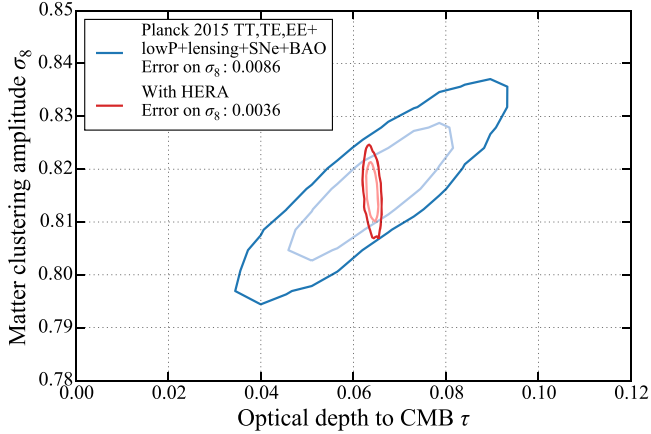
Figure 6. Likelihood contours (68% and 95%) for σ_8 and τ using *Planck* constraints (blue) and adding HERA data (red). The 21 cm constraints break the CMB degeneracy between the amplitude of density fluctuations and the optical depth, improving constraints on both.

only CMB data. HERA effectively reduces error bars on σ_8 by more than a factor of three (Liu et al. 2016), potentially elucidating current tensions between cluster cosmology constraints and those from primary CMB anisotropies.

2.2.2. First Images of the Reionization Epoch

In addition to measuring the power spectrum, there is the potential for HERA to directly image the IGM during reionization over the 1440 deg² stripe that transits overhead, which is comparable to future WFIRST large area near-IR surveys. After 100 hr on a single field (achievable in 200 nights), HERA reaches a surface brightness sensitivity of 50 μJy beam^{-1} (synthesized beam FWHM $\sim$ 24′) compared to the brightness temperature fluctuations of up to 400 μJy beam^{-1} in typical reionization models (see Figure 7). From the standpoint of sensitivity alone, HERA is capable of detecting the brightest structures at $z = 8$ with S/N > 10. Additionally, the design of HERA places it in a unique position to directly explore calibration techniques (e.g., redundant calibration, Liu et al. 2010; Zheng et al. 2014), while retaining a high quality point spread functions for imaging and identifying foregrounds. Additional details may be found in Carilli & Sims (2016).

2.2.3. Pre-reionization Heating

Prior to reionization, the 21 cm signal is a sensitive probe of the first luminous sources and IGM heating mechanisms. First stars are expected to form at $z \sim 25$–30 and their imprint on the 21 cm signal is expected to be sensitive to the halo mass where they are formed (Mesinger et al. 2015). The IGM is then expected to be heated by first generation X–ray binaries (Furlanetto 2006; Pritchard & Furlanetto 2007; Mesinger et al. 2013) or by the hot interstellar medium produced by the first supernovae (Pacucci et al. 2014), although the heating timing

and magnitude is still very much debated (Fialkov et al. 2012). Dark matter annihilation (Evoli et al. 2014) could also inject energy in the IGM, leaving its imprint in the 21 cm signal.

While the observational and analytical state of the art of pre-reionization 21 cm science is not as advanced as for the EoR (Ewall-Wice et al. 2016b), with the development of feeds sensitive down to 50 MHz, HERA will explore the IGM prior to reionization with a goal to constrain the sources of heating, obtaining, in the case of X–ray heating, percent-level constraints on the efficiency with which star-forming baryons produce X-rays (Ewall-Wice et al. 2016a). Lower frequency observations also test feedback mechanisms that interact with low-mass halos at high redshifts (Iliev et al. 2007, 2012; Ahn et al. 2012). Such constraints, while interesting in their own right, also reduce the susceptibility of the aforementioned 21 cm-derived τ constraints to uncertainties in high-redshift physics (Liu et al. 2016), especially if they are combined with upcoming or proposed measurements of the pre-reionization sky-averaged spectrum (Fialkov & Loeb 2016). Additionally, they may be crucial to a correct interpretation of kinetic Sunyaev–Zel'dovich effect constraints on reionization from the CMB (Park et al. 2013). The high redshift probe of structure afforded by the low frequency 21 cm measurements will permit some of the most direct observations of hypothesized suppressions of small-scale structure (Dalal et al. 2010; Tseliakhovich et al. 2011; Fialkov et al. 2012) arising from predicted supersonic relative velocities between dark matter and baryonic gas (Tseliakhovich & Hirata 2010). No other electromagnetic probe can provide direct observations of this epoch.

2.3. Other Scientific Objectives

Given its high sensitivity, frequency support, filled aperture and outriggers, HERA is capable of delivering more than the core 21 cm science discussed above. HERA will make the data available to the community after only a short quality assurance time period to help facilitate low-frequency science. Additionally, we encourage groups to leverage HERA as a platform upon which other equipments could be deployed. The Moore Foundation's support of HERA feed development and data analysis targeting the pre-reionization science described in Section 7 is a prime example of how we envision this functioning. Transients also provide an avenue for promising research. Below, we list examples of the broader science that HERA could impact.

2.3.1. Cross-correlations with Other Reionization Probes

HERA's public data provide new opportunities for cross-correlation studies. Cross-correlation between HERA 21 cm images and other high-redshift probes (e.g., *James Webb Space Telescope*; WFIRST; CMB maps; CO, CII, and Lyα intensity mapping) can provide an independent confirmation of the
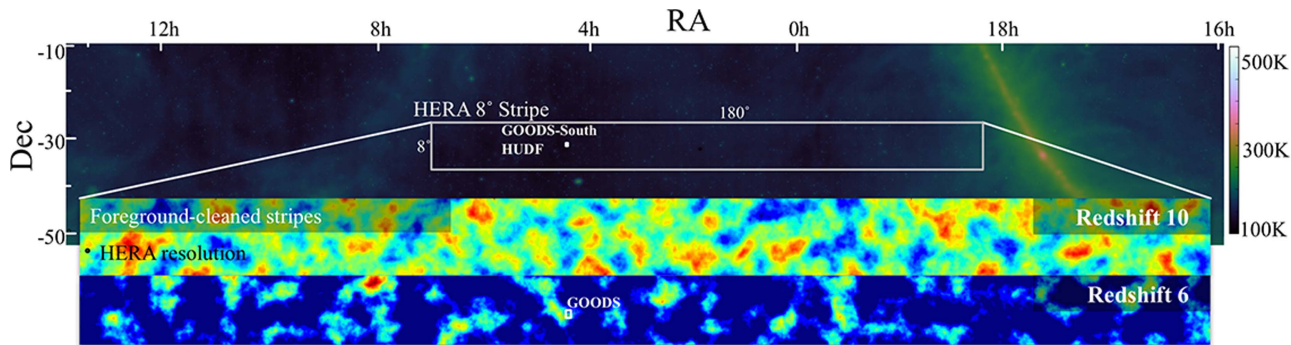
Figure 7. HERA will observe a 1440 deg^2 stripe centered near $\delta = -30°$. HERA can measure the ionization state around galaxies in, e.g., the GOODS-South field that contains a third of all known $z > 8$ galaxies. HERA's primary imaging data product to the community will be deep cubes along the HERA stripe suitable for cross-correlation.

(A color version of this figure is available in the online journal.)

21 cm power spectrum (i.e., Lidz et al. 2009; Pullen et al. 2014; Silva et al. 2015; Vrbanec et al. 2016) and enable rich new studies of the interaction between galaxies and their ionization environment. In particular, cross-correlating 21 cm with galaxy surveys can measure the characteristic bubble size around galaxies of different luminosities (Lidz et al. 2009) and help separate the degeneracy between the fraction of photons escaping the galaxies and the total number of ionizing photons produced (Zackrisson et al. 2013).

Fortuitiously, the GOODS-South field—one of the most panchromatically studied regions of the sky, the site of the Hubble UDF, and home to over a third of all known $z > 9$ galaxies—lies in HERA's field of view. HERA's images of the IGM can provide environmental context to galaxy surveys through identification of ionized bubbles (e.g., Malloy & Lidz 2013), or in a more statistical sense as described in Beardsley et al. (2015).

2.3.2. Searching for Exoplanetary Radio Bursts

HERA could revolutionize the study of extrasolar magnetospheres if it detects bright, highly polarized exoplanetary auroral radio bursts (Zarka 2011, p. 287). Observers have tried to detect these distinctive events since even before the discovery of the first exoplanet (Winglee et al. 1986) but have thus far not succeeded. The bursts occur at the electron cyclotron frequency and are highly beamed, allowing remote sensing of planetary rotation periods and magnetic field strengths, two quantities that are otherwise only indirectly measurable. Since magnetic fields may play a key role in protecting atmospheres and/or biospheres from energetic stellar wind particles (e.g., Tarter et al. 2007), studies of planetary magnetism may be vital to evaluating habitability. HERA's sensitivity, large field of view, long campaigns, and precise calibration make it well-suited to the search for radio bursts from Jupiter-like planets out to 25 pc. Well-studied exoplanet host stars in the HERA stripe within that

distance include Fomalhaut, Gl 317, Gl 433, Gl 667 C, and HD 147513.

2.3.3. Fast Radio Burst Followup

Fast Radio Bursts (FRB) are millisecond-long radio flashes whose origin has remained a great enigma ever since their discovery (Lorimer et al. 2007). HERA could be triggered by nearby, higher-frequency telescopes for FRB followup, saving baseband data and thus full sensitivity to all dispersion measures. This would require additional hardware, but the architecture allows for such additions. Bursts like that discovered by Masui et al. (2015), the lowest frequency FRB detection to date, should be seen hourly by HERA at 5–10σ. Observations at HERA frequencies are very sensitive to the physics of the intervening medium, particularly deviations from λ^2 dispersion. Detecting deviations would rule out broad classes of models and could indicate whether FRBs are at cosmological distances.

2.3.4. Continuum Imaging

Figure 8 shows a mock observation of the Galactic Center region. For the input model sky (color scale), we adopt the Effelsberg 1.4 GHz sky survey at $\sim 10'$ resolution and a pixel size of $4'$ (Reich et al. 1990). The model image is adjusted to Jy pixel^{-1}, and scaled to 130 MHz assuming a spectral index of -0.8. Noise is added per visibility assuming standard array parameters, and an integration time of 100 hr, and a bandwidth of 8 MHz. The thermal noise in the image in bright regions of the Galaxy would be about 100 μJy, however, at $12'$ resolution and 130 MHz the array is completely in-beam confusion limited at the level of a few Jy beam^{-1}. The resulting image is shown as the blue contours. See Carilli & Sims (2016) for more details.
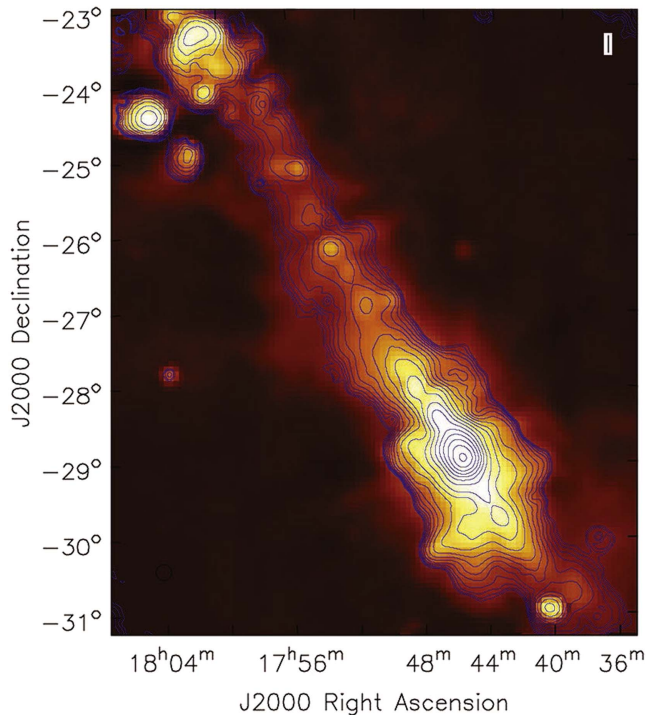
Figure 8. Color scale showing an input model image of the Galactic center region based on the Effelsberg 21 cm continuum survey (Reich et al. 1990). The contours show the mock HERA-350 observation at 130 MHz with a resolution of 12′. Contour levels are a geometric progression in square root 2, starting at 5 Jy beam^{-1}. The peak surface brightness on the HERA image is 2330 Jy beam^{-1}.

(A color version of this figure is available in the online journal.)

3. Measuring the EOR

Due to the expansion of the universe over cosmological time, we can identify and measure the early universe via the redshift of spectral lines. The hydrogen hyperfine transition at a rest frequency of 1420 MHz is a key spectral line due to the ubiquity of hydrogen and, being a "forbidden" transition, the optical depth lets us see through the entire universe back almost to the period of recombination. The bandwidth therefore equates to a cosmic distance along the line of sight of the telescope, with the frequency determining the cosmic age. An observation of an area of sky over a given bandwidth is therefore providing an average over a cosmic volume.

As the distance to the EOR is great (about 13 billion light-years) the signal is weak. However, the signal also subtends the entire sky, so initial measurements of the EOR strive to measure a statistical power spectrum of the signal over the sky since the nature of the reionization process should have a specific spatial signature. The goal is therefore to measure a range of aggregate spatial scales on the sky, rather than to image the signal directly. Imaging does remain an ultimate goal to fully understand the process, however we will likely need a
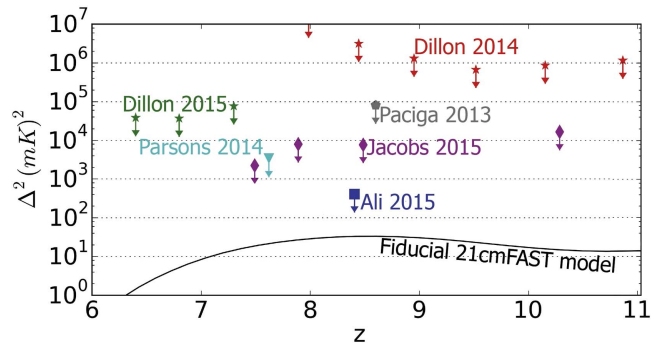

Figure 9. Current best published 2σ upper limits on the 21 cm power spectrum, $\Delta^2(k)$, compared to a 21 cm FAST-generated model at $k = 0.2\,h\,\mathrm{Mpc}^{-1}$. Analysis is still underway on PAPER and MWA observations that approach their projected full sensitivities; HERA can deliver sub-mK^2 sensitivities.

(A color version of this figure is available in the online journal.)

greater understanding of the signal characteristics and the systematics to achieve this more difficult goal.

Obviously between our present observation point and the EOR lies the entire intervening universe, which has an intrinsically much brighter signal (up to six orders of magnitude or more). Primarily, this power is due to diffuse Galactic synchrotron radiation, supernova remnants and extragalactic radio sources. As a first step, areas of the sky where these signals are minimal (for example, outside the galactic plane and away from strong point sources) are targeted (Bernardi et al. 2013). More importantly and most fortuitously however is the fact that all of these foreground signals are smooth spectrum sources whereas the expected spectrum of the EOR is expected to be rough since it is made up of non-ionized regions which are randomly distributed over a wide range of redshifts. This fact allows us to try and isolate foregrounds from the EOR, as will be discussed.

As seen in Figure 9, the past three years have seen deep EOR observations with PAPER, the MWA, the Giant Metrewave Radio Telescope (GMRT), and LOFAR. PAPER and the MWA have produced progressively deeper limits (Dillon et al. 2014, 2015a; Parsons et al. 2014; Ali et al. 2015), with PAPER yielding the first meaningful constraints on the 21 cm spin temperature during reionization. The inherent challenge is to simultaneously meet stringent sensitivity requirements while suppressing foregrounds ∼5 orders of magnitude brighter than the 21 cm signal, which has been addressed along a number of approaches. To address this challenge, all aspects of the experimental process must be refined and improved, spanning calibration (e.g., Zheng et al. 2014; Barry et al. 2016; Jacobs et al. 2016), handling foreground contamination (e.g., Moore et al. 2013; Thyagarajan et al. 2015a, 2015b; Pober et al. 2016), and the interferometer design itself (e.g., Parsons et al. 2012a; Dillon & Parsons 2016).

A promising approach to make the first detection of the EoR power spectrum is a foreground mitigation strategy based largely on identifying and filtering out a region of parameter space where the strong foregrounds are largely confined (Section 3.2). This is the approach pioneered by PAPER. By reducing the need for foreground modeling and subtraction, this approach allowed PAPER to switch to a grid-based antenna layout that enhanced sensitivity toward fewer Fourier modes and facilitated calibration based on the "redundancy" of different antenna pairs measuring the same sky modes (Liu et al. 2010; Zheng et al. 2014). Combined, redundancy and delay filtering provide a robust, inexpensive, and demonstrably successful solution to the foreground problem.

Yet PAPER's lack of imaging support and its uneven *uv* sampling leave it with limited diagnostic capability, particularly for direction-dependent systematics such as polarization leakage from Faraday-rotated emission (Moore et al. 2013; R. Nunhokee et al. 2016, in preparation). While concern over such effects has decreased markedly since discovering that intrinsic point source polarization is lower than previously thought (Bernardi et al. 2013; Asad et al. 2015) and that variable Faraday rotation through the ionosphere averages down the polarized signal over long observing seasons (Aguirre et al. 2016; Moore et al. 2016), direction-dependent beam effects remain an area of interest. The MWA's image-based calibration and foreground subtraction strategy provides complementary capabilities (Section 3.3). Imaging with subtraction, while still under development as a viable foreground strategy, can increase sensitivity by recovering more modes of the cosmological signal (see Table 1) and help address systematic errors rooted in the image domain. HERA's antenna configuration—shown in Figure 21 and discussed in Section 5.3 —emphasizes the proven approaches of redundant calibration and delay filtering, while simultaneously increasing the extent and density of *uv* sampling for high-fidelity imaging.

Despite progress, the fact remains that the 21 cm EoR signal is intrinsically very faint; making a detection requires a large instrumental collecting area and a long, dedicated observing campaign. Although published PAPER and MWA results (Figure 9) do not yet include observations at full sensitivity that are still being analyzed (e.g., Figure 4), it is clear already that these instruments lack the sensitivity to make a conclusive detection (see Table 1). HERA addresses this shortcoming with a dish element that delivers a much larger collecting area while retaining the necessary characteristics for both proven and forward-looking foreground removal strategies.

This section will provide a brief overview of the theoretical underpinning of how foregrounds contaminate the measurement (the so-called "wedge"), discuss the various techniques used to make the measurement and finally provide a brief discussion on calibration issues and techniques.

3.1. The "Wedge"

Perhaps the most important advance informing HERA's design is a refined understanding of how smooth-spectrum foregrounds interact with instrument chromaticity to produce a characteristic "wedge" of foreground leakage in Fourier space (see Figure 10), outside of which the 21 cm signal dominates (the "EOR window"). The wedge is a direct consequence of the chromatic response of an interferometer. Through theoretical and observational work (Datta et al. 2010; Morales et al. 2012; Parsons et al. 2012b; Vedantham et al. 2012; Hazelton et al. 2013; Pober et al. 2013a; Thyagarajan et al. 2013; Liu et al. 2014a, 2014b), we have learned how the boundary between the wedge and the EoR window is determined by the separation between antennas, signal reflections within antennas, and the angular response of the antenna beam. Deep integrations also show us that, to the limits of current sensitivity, intrinsic foreground emission is absent outside of the wedge; it can only appear there through instrumental leakage (Parsons et al. 2014; Ali et al. 2015; Kohn et al. 2016; Moore et al. 2016; Thyagarajan et al. 2016).

The power spectrum measurement provides the spatial correlations across the sky, characterized by the magnitude of the wavenumber, $\boldsymbol{k}$. Though the full magnitude of the $\boldsymbol{k}$-vector is used, it is instructive to split it into two components, $\boldsymbol{k} = \boldsymbol{k}_\perp + k_\parallel \hat{z}$ where $|\boldsymbol{k}_\perp| \equiv k_\perp = 2\pi b / \lambda X$ is determined by the antenna baseline (b) and $k_\parallel = 2\pi / (YB)$ by the bandwidth (B). Here X and Y are cosmological parameters relating angular size and spectral frequency to cosmic volumes respectively (so, relating wavenumber to physical volume at a given redshift). $\boldsymbol{k}_\perp$ corresponds to the plane of the sky and $k_\parallel$ to the line of sight. This is useful since it allows us to split the chromatic response of the interferometer visibility measurement from the instrument bandpass and isolate a phase space where smooth-spectrum foreground sources (i.e., everything *not* the EOR) contaminate the signal of interest from where they do not.

As just stated, the $\boldsymbol{k}_\perp$ components are directly proportional to the baselines and $k_\parallel$ are proportional to the Fourier transform of the frequency response.[18] The Fourier transform of a frequency spectrum is a delay spectrum, hence the "delay-spectrum" moniker for the technique that uses this approach. Note that cosmic evolution limits the largest bandwidth (which determines the smallest $k_\parallel$) to about 10 MHz—for larger bandwidths the evolution of the universe begins to impact the result. For HERA, wavenumbers are dominated by the bandwidth, not the baseline.

Figure 11 shows many of the dependencies on wavenumber of the bandwidth, configuration and cosmology by plotting the perpendicular wavenumber ($\boldsymbol{k}_\perp$; black lines), parallel wavenumber ($k_\parallel$; blue lines) and total wavenumber (k; green lines) as

---

[18] Note that this equivalency is an approximation, which is very good for the short baselines and small bandwidths generally used here. For a more complete discussion see Liu et al. (2014a, 2014b).
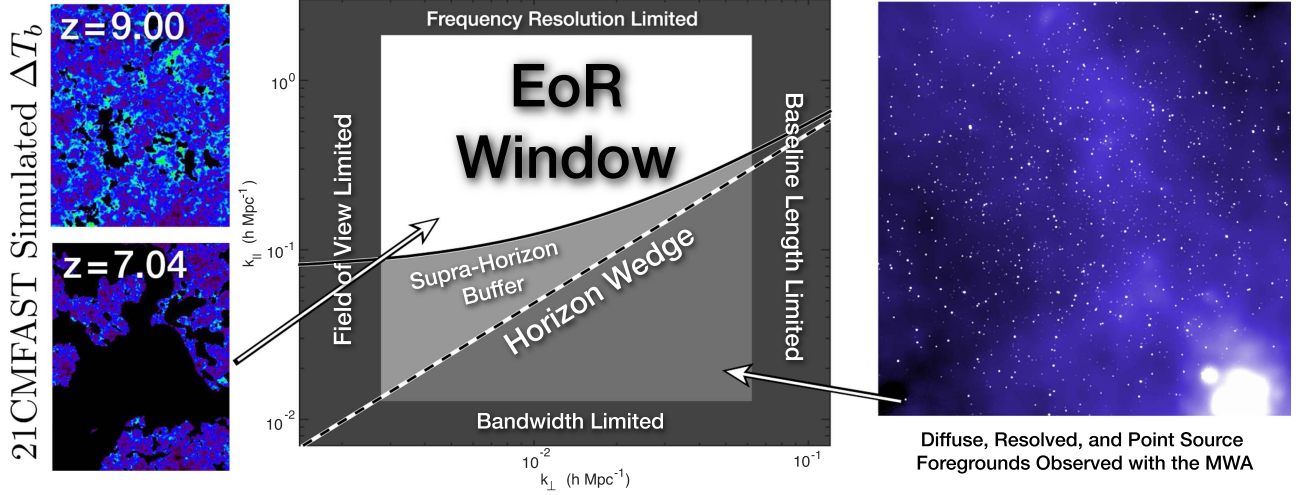
Figure 10. Foregrounds are a primary challenge facing 21 cm cosmology experiments. HERA leverages a "wedge" in the cylindrically averaged (k is broken into $k_\parallel$ and $k_\perp$) power spectrum (center panel). Smooth-spectrum foregrounds (right panel) ∼3–5 orders of magnitude brighter than fiducial EoR models (left panel; Mesinger et al. 2011) create the "wedge" when they interact with the interferometer's chromatic response. Flat spectrum foregrounds cannot contaminate the EoR window beyond the horizon wedge, though intrinsic or imperfectly calibrated chromaticity can push it slightly beyond the horizon. By avoiding foregrounds, PAPER has placed limits within an order of magnitude (in mK) of these models (Ali et al. 2015) and shown the "EoR Window" to be foreground-free. HERA's dish and compact configuration optimize wedge/window isolation and direct sensitivity to low-$k_\perp$ modes where the EoR is brightest relative to the foreground wedge. (A color version of this figure is available in the online journal.)

a function of redshift for various bandwidths and baselines. The redshift range is appropriate for the extended frequency range that is the goal for HERA, however $z = 6$–13 is the primary region for EOR studies. The lines are labelled for the assumed bandwidth and/or baseline, depending on the type of wavenumber shown. Obviously many values may be used, but here a small sampling of values appropriate for HERA are shown. Wavenumbers with an assumed bandwidth (k and $k_\parallel$) are shown as stepped profiles, with the redshift steps equal to the bandwidth at that redshift. Note that for 100 MHz, the concept of a power spectrum at a given redshift is no longer appropriate, which is why the line is dashed. Also in Figure 11, the lime-green shaded area indicates the initial region in which HERA intends to detect and characterize the EOR using the delay-spectrum technique.

Note that the unit of the spatial wavenumber k is length^{-1}, in this case the relevant length scale is megaparsecs (Mpc; 1 Mpc = 3.086×10^{22} m). In order to account for updated measurements of the present-day Hubble parameter H_0, it is further normalized by a factor h, where $H_0 = 100h$ (km s^{-1})/Mpc, such that the wavenumbers are expressed in units of h Mpc^{-1}. Also note that at the redshifts of interest X has a value of about 160 Mpc deg^{-1} and Y has a value of about 16 Mpc MHz^{-1}.

In these variables, the "contaminated" phase space is a wedge-shaped region in $k_\perp - k_\parallel$ space such that the ratio of the time-delay across a given baseline (b/c, which impacts chromatic visibility) and the delay associated with a given

bandwidth ($1/B$) is less than some parameter determined by the details of the system, which we denote as $1/\beta$. Substituting $k_\perp$ and $k_\parallel$ in for b and B in this ratio, this wedge is bounded by

$$k_\parallel \leqslant \beta \frac{X\lambda}{Yc} k_\perp + \frac{S}{Y}, \tag{1}$$

where an offset parameterized by S accounting for effects related to the combined spectral smoothness of the foregrounds and the antenna response has been included (see Figure 10). The impact of this offset parameter is explored in Thyagarajan et al. (2013).

If this β factor is determined solely by the chromaticity of the longest baseline, we see that $\beta = 1$ and this line is referred to as the "horizon line" (i.e., the delay of a source at the horizon). Systematics will push that line such as to close the EOR "window" to the upper left ($\beta > 1$). If we can completely control systematics and constrain the effects of the foreground to e.g., the main beam, the line will move to decrease the size of the wedge ($\beta < 1$). Therefore, a key issue to measuring the EOR power spectrum is to understand and minimize systematics. For further discussion and an analytical derivation, see Vedantham et al. (2012), Thyagarajan et al. (2013), Liu et al. (2014a) and Liu et al. (2014b). In simulations see Datta et al. (2010) and Hazelton et al. (2013), and for observations Pober et al. (2013a), and Parsons et al. (2014).

The techniques to measure the power spectrum may be broken down into two principle techniques—delay-space
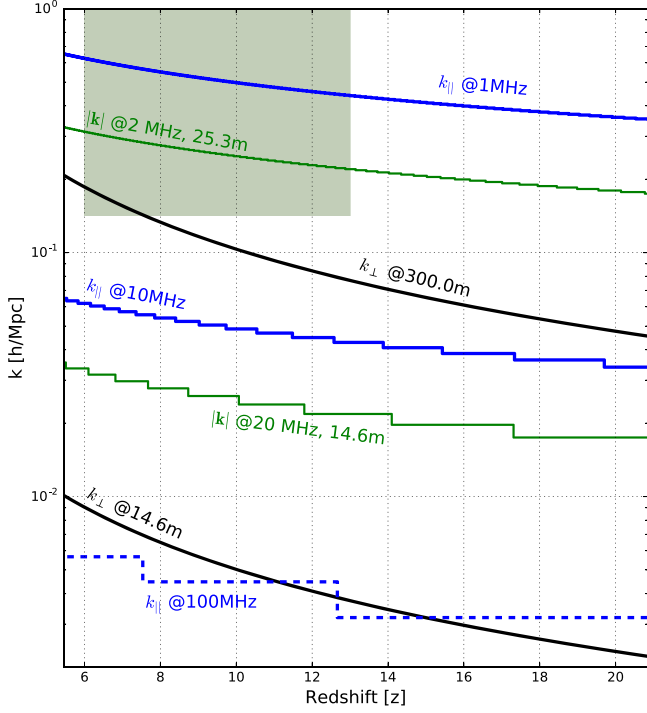
Figure 11. $|k|$, $k_{\parallel}$, $k_{\perp}$ wavenumber plots at various bandwidths ($k_{\parallel}$; blue), baselines ($k_{\perp}$; black), and total ($|k|$; green) as a function of redshift. The stepped profiles for $k_{\parallel}$ and $|k|$ are the line of sight redshift ranges for that bandwidth (too small to see at 1 MHz). See text for discussion. The full redshift range is the HERA extended goal. The initial HERA delay-spectrum power spectrum goal is the light green square region in the upper left.

(Section 3.2) and map-making (Section 3.3)—plus additional hybrid methods. These are briefly summarized below, with an emphasis on the delay-spectrum technique as the initial approach taken by HERA. Finally, we provide a short discussion on calibration in the concept of this design.

3.2. Delay-spectrum Approach

Given that the response of an interferometer natively measures the power in Fourier modes of the sky within its beam, we see that it is a natural instrument to use for this measurement of the EOR spatial power spectrum. The delay-spectrum approach leverages the interferometer measurement to optimize sensitivity to the desired modes while rejecting modes contaminated by the foreground power in the wedge. Other than potentially handling overlapping bins in uv space, the delay-spectrum approach does not combine baselines before squaring and calculating the power spectrum, which contrasts to the map-making techniques briefly described in the following section. For more details, see Parsons et al. (2012b).

We can approximate the sky power spectrum $P(k)$ as being linearly proportional to the Fourier transform along the frequency axis (the delay-transform) of an interferometer

baseline visibility, denoted $\tilde{V}_b(\tau)$:

$$P(k) \approx \frac{X^2 Y}{4k_B^2}\left[\frac{\tilde{V}_b^2(\tau)}{\Omega_b B / \lambda^4}\right] \qquad (2)$$

where X and Y were introduced above, Ω_b is the integrated beam response, B is the effective bandwidth, λ is the observation wavelength, and k_B is Boltzmann's constant. The terms in square brackets are instrumental terms, as opposed to the constants and cosmological parameters out front. Rather than $P(k)$, the literature generally works with a volume-normalized parameter given by $\Delta^2(k) = \frac{k^3}{2\pi^2} P(k)$.

Since the thermal noise per visibility baseline may be expressed as

$$V_N = \left(\frac{2k_B}{\lambda^2}\right)\left(\frac{T_{\text{sys}}}{\sqrt{2Bt}}\right)\Omega_b B, \qquad (3)$$

where t is the integration time (see e.g., Thompson et al. 2001), to determine the sensitivity of an instrument to the power spectrum per baseline we can substitute the thermal noise per baseline for the visibility in Equation (2). Further, since an interferometer typically measures many baselines which may be averaged together to improve the signal-to-noise per k-bin, the total sensitivity may be approximated as

$$\Delta_N^2(k, z) \approx \frac{k^3 X^2 Y}{4\pi^2}\left[\frac{T_{\text{sys}}^2 \Omega_b}{t \mathcal{N}}\right], \qquad (4)$$

where $\mathcal{N}$ represents the improvement in sensitivity based on the array configuration, which may significantly boost the sensitivity if optimized for this measurement (see Parsons et al. 2012b).

Figure 12 (left) plots this "redundancy boost" factor for various configuration types relative to an array in a 19-element hexagonal configuration. They are labelled for the type of configuration (*hex, grid, imaging*) and the number of antennas (from 37 to 350). Note that (a) *hex* is based on the configuration used for HERA (14.6 m center-to-center spacing); (b) *grid* for that of PAPER (4 m N–S, 16 m E–W spacing); (c) *imaging-128* for MWA (Tingay et al. 2013); and (d) *imaging-48* for LOFAR (van Haarlem et al. 2013; note that this assumes the ability to fully correlate the HBA-pairs in the Netherlands core). The plot shows that for a fixed number of elements using the delay-spectrum approach, redundant arrays (*hex* and *grid*) provide about an order of magnitude improvement over imaging arrays. Since the baselines go as order N^2, this corresponds to using about $1/3$ of the number of elements to yield the same performance (as verified by the *Hex-37/Imaging-128* lines). This specific dependency does not extend to the other approaches discussed below and imaging configurations would likely be preferred. Note that a filled hexagonal-packed array provides excellent imaging as well, but with potentially limited resolution unless outriggers are included.
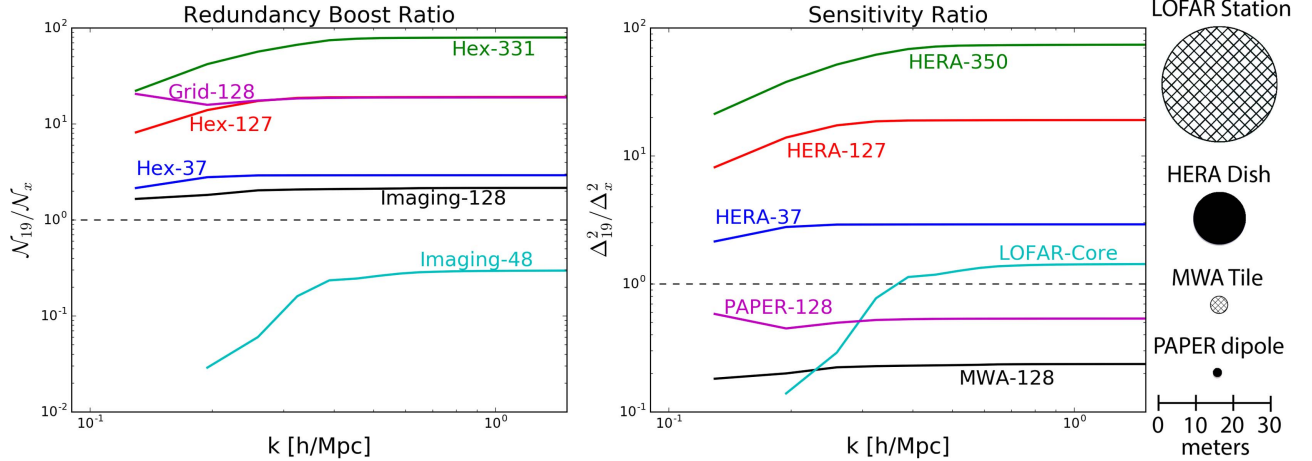
Figure 12. Left: representative boost factors ($\mathcal{N}$ in Equation (4)) normalized to a 19-element hexagonal configuration spaced at 14.6 m. For a given element count, one can get about an order of magnitude improvement in delay-spectrum sensitivity. Alternatively, for the same sensitivity one can build roughly $1/3$ the antennas. Right: power spectrum sensitivities for various arrays normalized to HERA-19. The element sizes are indicated at the far right with appropriately sized circles. Cross-hatching denotes phased tiles.

(A color version of this figure is available in the online journal.)

Another approach to improving sensitivity is to make the collecting area per element larger. A larger element does limit the accessible field of view, but this is not a huge liability for a focussed experiment as long as an appropriate patch of "cold" sky passes within its field of view and a large enough piece of sky is surveyed to overcome sample variance. These conditions hold true for HERA. Figure 12 (right) shows the relative sensitivity incorporating configuration and element size of various arrays relative to HERA-19 using 21cmSense, calculated for a redshift corresponding to the peak signal at a hydrogen reionization fraction of 0.5 (in this case, $z = 8$). The circles to the right indicate the relative sizes of the elements. Note that MWA and LOFAR are cross-hatched to indicate phased array tiles, which uses small antennas to phase up a full element response.

As an aside, we can compare and contrast the delay-spectrum technique to imaging with an interferometer. For imaging, one takes a 2D spatial Fourier transform of the visibilities, and produces images as a function of frequency. Here, one is taking a 1D Fourier transform along the other axis (the bandpass) and produces a 3D spatial power spectrum. In imaging, point sources are transformed to a single pixel, whereas for the delay-spectrum, smooth sources are transformed to a single delay. For imaging, we are concerned with ripples in the passband due to standing waves, whereas for the delay-spectrum we are concerned with delayed versions of the signal due to multiple reflections (equivalent views of the same phenomena).

3.3. Mapmaking Approach

In contrast to the delay-spectrum approach, mapmaking approaches combine baselines to build up information before squaring and calculating the power spectrum. The conceptually simplest approach is to first make an image cube of the sky as a function of angular position and frequency, take the spatial Fourier transform, square and bin the cube, then subtract the dominant foreground power and take the transform to determine the EOR power spectrum (Liu & Tegmark 2011; Dillon et al. 2013). The image domain is a natural place to combine information from partially coherent pairs of visibility measurements (either from different baselines or from the same baseline at different times). Mapmaking can be a lossless data compression step (Tegmark 1997), though keeping track of statistical properties of the maps, which have complex frequency and position dependent point spread functions and noise covariance matrices, can be computationally challenging (Dillon et al. 2015b). Existing approaches have had to make a number of approximations, including that point spread functions do not vary over the field of view and that noise is not correlated between uv-cells. Additionally, mapmaking is in principle not as vulnerable to polarization leakage as the delay-spectrum approach, since only polarization mismodeling (rather than any kind of polarization asymmetry) can cause leakage from Stokes Q or U to I.

One advantage of such an approach is that sky images can be interesting in their own right, both for dealing with measurement systematics and for accessing the non-Gaussian

observational signatures (such as ionized bubble structures) that are missed by variance statistics such as the power spectrum. Mapmaking also allows for the direct subtraction of bright foregrounds, potentially expanding the EoR window. However, accessing these high-order statistics or the modes of the power spectrum inside the wedge using a mapmaking approach requires extreme (and so-far undemonstrated) precision in calibration and forward-modeling of bright foreground models through instrument systematics. For this reason, the approach is to detect and initially characterize the power spectrum via the delay-spectrum technique while developing tools for other approaches.

3.4. Hybrid Approaches

While they were presented separately above, the delay-spectrum and map-making approaches need not be viewed as mutually exclusive. For example, mapmaking does not nned to be limited to the real space image basis; pipelines that combine multiple baselines into estimates of various Fourier amplitudes of the sky are formally also mapmaking pipelines. Like the delay-spectrum approach, such pipelines (see, e.g., Trott et al. 2016) avoid the image domain entirely. This helps to prevent artifacts that may be introduced by imaging algorithms.

More generally, it is possible to express a mapmaking algorithm as a linear operator that acts on visibility data to produce a compressed dataset (Dillon et al. 2015b). It follows then that squaring this to obtain an estimate of the power spectrum then results in a weighted quadratic combination of visibilities, where one multiplies the visibility from every baseline with that from every other baseline. These visibility product pairs are subsequently normalized to form their own individual estimates of the power spectrum before all the normalized pairs are summed together to form a final power spectrum. Measuring a power spectrum in this way combines the best aspects of the mapmaking and delay-spectrum approaches. Power spectra are formed directly by the cross-multiplication of visibility data, preserving the delay-spectrum approach's strategy of staying close to quantities measured by an interferometer; on the other hand, by multiplying together the data from every possible combination of baselines, one retains all the information from partially coherent visibility pairs captured by mapmaking. Indeed, it can be shown (Liu et al. 2014a) that in the limit of infinitely fine Fourier space bins, the hybrid method is mathematically equivalent to the mapmaking approach. In practice, the hybrid method comes with the added benefit of allowing particular baseline pairs that are suspected of being affected by instrumental systematics to be more surgically downweighted. However, similar to map-making techniques, these approaches need much additional precision in calibration and modeling development in order to be implemented with confidence.

Fundamentally, the hybrid approach and the optimal mapmaking approach (Dillon et al. 2015b) are very similar. Whether it makes computational sense to examine all pairs of partially coherent visibilities or to perform mapmaking as an intermediate data-compression step before power spectrum estimation (despite the complexity of the resultant map statistics) is an open question that depends on a number of factors, including the number of elements in the array, its layout, and its integration time.

3.5. Calibration

As examined above, maximizing sensitivity to a limited number of spatial modes for the delay-spectrum technique requires a grid of antennas that simultaneously measures the same baselines using many redundant pairs of antennas. This redundancy may also be exploited to calibrate the array as well, as long as the true antenna positions fall close enough to that ideal grid (Liu et al. 2010). This technique was pioneered with the MITEoR experiment (Zheng et al. 2014), and has resulted in a package called OMNICAL developed for PAPER and HERA (https://github.com/jeffzhen/omnical). Ali et al. (2015) provide a description of this technique as it applies to calibrating the PAPER array, which is mostly situated on a grid with many redundant baselines. This section provides a high-level overview of such calibration as it applies to HERA.

Fundamentally, the problem of calibration is the determination of a complex, frequency-dependent gain for each antenna which arises due to differences in amplifiers, cables, etc. Given those gains, the visibility measured by antennas i and j at frequency ν is given by

$$V_{ij}^{\text{measured}}(\nu) = g_i(\nu) g_j^*(\nu) V_{ij}^{\text{true}}(\nu), \qquad (5)$$

where each $V_{ij}(\nu)$ is the measured or true visibility and $g_i(\nu)$ is the gain on antenna i at frequency ν.[19] With its highly redundant array configuration (see Section 5.3), HERA's 350 antennas measure 61,075 visibilities, but only 6140 unique baselines. Given a set of measured visibilities, it is possible to estimate both the 6140 unique true visibilities and the 350 complex gains simultaneously because that system of equations is greatly overdetermined. A method for linearizing the system and applying standard minimum-variance linear estimators was developed by Liu et al. (2010) and first applied in Zheng et al. (2014). Unlike traditional calibration of radio interferometers, redundant calibration makes no reference to any sky model, requiring merely that the sky is bright relative to the noise on each antenna (which is always true in the sky-noise dominated regime characteristic of 21 cm observatories with wide fields of view).

---

[19] This discussion ignores electromagnetic cross-talk between antennas and antenna-to-antenna variation of the primary beam.

However, at each frequency, degeneracies in the redundant calibration procedure prevent it from solving four numbers per frequency for the whole array (down from 700 in HERA's case if full calibration, as opposed to redundant calibration, were needed). The first is an overall gain—for example, one can multiply each $g_i(\nu)$ by 2 and divide each $V_{ij}^{\rm true}$ by 4 and get exactly the same measured visibilities. The others are an overall phase and two other phase terms that describe the tip and tilt of the array. These degeneracies mean that the output of any redundant baseline calibration also need to undergo a final, "absolute" calibration.

4. High-level Requirements

From the science and techniques discussed above, we may derive some high-level requirements predicated on optimizing for the delay-spectrum approach of detecting the EOR power spectrum while not unduly limiting other approaches or other science goals. The fact that HERA is an experiment and not meant to be a long-term general use facility greatly facilitates this optimization. This section describes the element, configuration, frequency and sensitivity requirements that largely set the overall design concept.

4.1. General Antenna Design and Configuration

The primary new feature of HERA over previous generation experiments (in this context primarily PAPER) is the use of large elements to increase the sensitivity, as indicated in Figure 12. The cost-performance optimization will be discussed below, however we see that to address the central challenges of the delay-spectrum approach in the context of the wedge HERA should use close-packed antennas that minimize signal reflections over long delays and deliver significant forward gain relative to their horizon response. Tests with prototype HERA antennas (Figures 14 and 16, discussed in Section 5.2) indicate that a moderately large parabolic dish with a short focal height can meet these requirements (Ewall-Wice et al. 2016b; Neben et al. 2016; N. Patra et al. 2016, in preparation; Thyagarajan et al. 2016). Note that to pursue map-making and hybrid techniques, additional antenna outriggers are valuable additions, so the design should be able to accommodate ≈1 km baselines. Note that in referring to the EOR sensitivity of the array, often the number of antennas just in the core are indicated—that is for EOR HERA-320 and HERA-350 are often used interchangeably.

4.2. Frequency and Bandwidth

Figure 2 indicates the frequency range requirement to probe the expected timescale of the epoch of reionization using the 21 cm line of hydrogen as the probe. These limits are derived from to-date complementary probes of reionization which include measurements of the optical depth to last scattering in

the CMB, QSO spectra, Lyα absorption in the spectra of quasars and gamma-ray bursts and the demographics of Lyα emitting galaxies (Figure 3). Constraints from these probes are still weak: Lyα absorption saturates at very small neutral fractions; galaxy surveys directly constrain only the bright end of the luminosity function and depend on an unknown escape fraction of ionizing photons to constrain reionization; CMB measurements probe an integral quantity subject to large degeneracies Even when these observations are combined into a single 95% confidence region, the bounds remain weak. For example, $x_{\rm H\,I}$ spans almost the entire allowable range of [0, 1] at $z = 8$. Twenty-one centimeter reionization experiments place much tighter constraints on ionization, with the red band showing the forecasted 95% confidence region derived from HERA data, after marginalizing over astrophysical and cosmological parameters.

From these measurements and models, HERA is required to cover a redshift range of $z = 6$ to 13, corresponding to a frequency range of 101–203 MHz. We adopt 100–200 MHz for full performance as the requirement. Extending the science to include the Dark Ages remains a goal so that efforts are on-going to design a feed to increase the lower limit down to 50 MHz without compromising the performance in the above requirement range. The fall-back position for low frequencies is a serial deployment of a scaled version of the HERA feed or to potentially build additional elements specifically for low frequencies.

The scientific requirement on channel bandwidth is to allow access to k-modes of $\sim 1\,h\,{\rm Mpc}^{-1}$, which requires about 256 channels over the 100 MHz bandwidth. However, in order to handle radio frequency interference as well as to allow the bandpass to be characterized, a specification of 1024 channels has been chosen. This yields a channel bandwidth of 97.7 kHz.

The total simultaneously processed bandwidth is the full 100 MHz, since we wish to efficiently probe the entire redshift range. The main impact from this requirement is the bandwidth from the digitizer back to the correlator, however this bandwidth is easily handled with current generation digital back-ends and will be greater than 100 MHz.

4.3. Delay Response

Early analysis (DeBoer & Parsons 2015) indicated that to trace the EOR over a wide range of redshift, internal reflections should be attenuated by about 60 dB from the initial incoming wave by about 60 ns, or a voltage standing wave ratio (VSWR) < 1.002 for frequencies <17 MHz. This was a conservative value based on estimates of power in spectrally smooth foreground sources (Santos et al. 2005; Ali et al. 2008; de Oliveira-Costa et al. 2008; Jelić et al. 2008; Bernardi et al. 2010) and experience with PAPER dealing with foreground systematics. This provided the basis for the initial design of the element. For the contemplated feeds on a primary focus
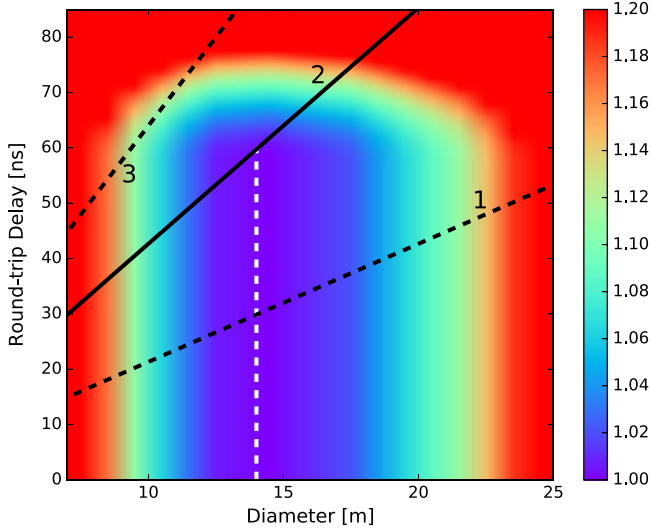
Figure 13. Background coloring with color bar shows the relative cost/performance for delay and cost at a fixed performance as a function of element diameter. See Sections 4.3, 4.4 and DeBoer & Parsons (2015) for details. A diameter of 14 m (vertical dashed line) is near the cost minimum and consistent with assumptions for the delay specification.

(A color version of this figure is available in the online journal.)

Figure 14. Antenna delay attenuation specification with realistic foregrounds from Thyagarajan et al. (2016). The blue, green and red lines show the maximum attenuation needed at a given delay for the foregrounds to be below the expected EOR signal level for different $k_\parallel$. The lower lines are for the worst case with no additional processing, while the dashed line assumes inverse covariance weighting. The teal line is the 60 dB by 60 ns initial conservative specification. HFSS calculations (black line) for the expected attenuation show the HERA dish meeting the more sophisticated specification for $k_\parallel \gtrsim 0.15\,h\,\mathrm{Mpc}^{-1}$.

antenna, it was found that a focal length/diameter radio (f/D) of approximately 0.32 was optimal. We may therefore estimate the attenuation as a function of delay and diameter and assign this a "cost function."

Figure 13 summarizes the adopted cost function augmented with an actual cost scaling. The vertical axis shows a steep delay "cost" at 60 ns and the horizontal axis shows the cost/performance model as a function of element diameter, as described in Section 4.4. The color coding is the product of the two assigned costs, with red showing a high cost normalized to 350 14 m elements (clipped at a ratio of 1.2) and purple being the minimum. The black lines labelled "1," "2" and "3" are the round-trip travel times for 1, 2 and 3 reflections between the feed and the vertex.

To try and obtain 60 dB by 60 ns we may interpret the black delay lines in Figure 13 in one of two ways: (a) a fixed attenuation/reflection determines what diameter is required, and (b) a fixed diameter determines how much attenuation per reflection can be allowed. Interpreting Figure 13, for one feed-vertex-feed round-trip and the assumed $f/D = 0.32$ over the diameters of interest, all delays are less than 60 ns. We therefore do not have to reduce the reflections to the extreme amount needed to get to 60 dB of attenuation within one round-trip. If we want to be able to handle two round-trips worth of delay, the diameter should be less than 14.2 m, which is near the cost minimum. Alternatively, if we assume 14.2 m, then we can estimate that each reflection must average a return loss better than 15 dB, an aggressive target. And finally, if we need
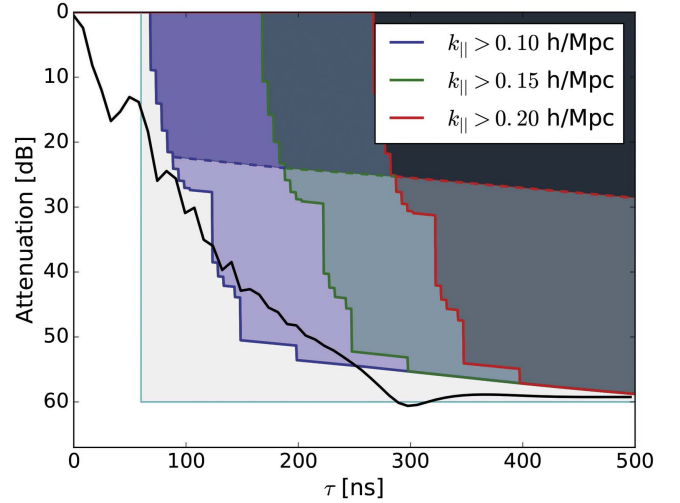
to allow for three round-trips, the antenna diameter would have to be less than 9.4 m, where the cost is quickly rising. To handle the delay requirement therefore, the diameter should be less than 14.2 m, or the return loss specification becomes very aggressive.

As a key specification, this has been a focus of study with a series of prototypes and analyses based on modeling, and measurements have been conducted to provide much more rigor than this early specification (Neben et al. 2016; N. Patra et al. 2016, in preparation; Thyagarajan et al. 2016). The simple specification set above more appropriately becomes a series of curves for attenuation and delay at different wavenumbers for realistic foreground model, as discussed below.

The more detailed specification is shown in Figure 14, adapted from Thyagarajan et al. (2016), showing the modeled results at $k = 0.10$, 0.15, and 0.20 $h\,\mathrm{Mpc}^{-1}$ (blue, green and red respectively) for the adopted design for two different cases. If the system attenuation as a function of delay (black line in figure) is greater than the attenuation needed to measure a specific $k_\parallel$ based on a realistic foreground model, the measurement should be free from foregrounds at the level of the expected EOR power for those wavenumbers and larger. The case extending down to ~55 dB is the worst case for the raw system with no additional processing. The dashed line at ~25 dB is for application of an inverse covariance weighted optimal quadratic estimator of the data (Patra et al. 2016, in preparation). The analysis shows that for the worst case the

dish design should allow for EOR detections for $k \gtrsim 0.15\,h\,\mathrm{Mpc}^{-1}$, while covariance weighting should allow detections at $k \gtrsim 0.10\,h\,\mathrm{Mpc}^{-1}$. We also see that the initial simple 60 dB by 60 ns specification was overly conservative (shown as the lightly shaded area bounded by the teal line), however it served as a good driving goal.

4.4. Sensitivity Optimization

As an instrument to characterize the power spectrum over the evolution of the EOR, the specification on sensitivity is to make at least a nominal detection over the redshift region of support ($z = 6$–13) along with a very robust detection at the peak. As seen in Figure 4 and Table 1, an array comprising 320 14 m core antennas (labelled HERA-350, which includes the outriggers) has sensitivity to a fiducial reionization model across that redshift range. We therefore adopt the delay-spectrum power spectrum sensitivity of 320 14 m close-packed antennas as the minimum sensitivity. For this sensitivity, the number of elements needed for a given diameter is

$$N_{\mathrm{core}} = (320 * 14)/D, \qquad (6)$$

where N_{core} and D are the number of antennas in the core and their diameter respectively. Note that the linear number-diameter dependence was derived by running multiple sensitivity codes (e.g., 21cmSense) over a range of values for the HERA configuration for wavenumbers greater than $0.15\,h\,\mathrm{Mpc}^{-1}$. This dependency differs from Mellema et al. (2013) and analytical expressions, mostly likely due to the assumed configuration. Optimization is therefore done for this sensitivity against cost for various diameters and total element numbers, while trying to minimize multiple reflections on long delays.

To determine this optimal diameter, full system costings were done on a range of diameter sizes from 5 to 25 m, with the total number set by Equation (6). This included the full system, except the post-processing (that is, everything after the archived correlator output). The costing information in Figure 13 is shown as the colored background oriented along the horizontal axis, recalling that the total "cost" function is the product of the actual costing and the delay-attenuation curve. The resulting normalized system cost/performance-curve becomes very flat (colored dark blue/purple) for diameters between about 12 and 15 m, which is consistent with the chosen value of 14 m based on other system considerations.

5. System Design

As described in the previous section, the critical insights from the first generation 21 cm EOR experiments have been applied to define the requirements for HERA—an instrument designed to ensure that foregrounds remain bounded within the wedge while delivering the sensitivity for high-significance detections of the 21 cm reionization power spectrum with

Table 2
HERA-350 Design Parameters and their Observational Consequences

Instrument Design Specification	Observational Performance
Element Diameter: 14 m	Field of View: 9°
Minimium Baseline: 14.6 m	Largest Scale: 7°.8
Maximum Core Baseline: 292 m	Core Synthesized Beam: 25′
Maximum Outrigger Baseline: 876 m	Outrigger Synthesized Beam: 11′
EOR Frequency Band: 100–200 MHz	Redshift Range: $6.1 < z < 13.2$
Extended Frequency Range: 50–250 MHz	Redshift Range: $4.7 < z < 27.4$
Frequency Resolution: 97.8 kHz	LoS Comoving Resolution: 1.7 Mpc (at $z = 8.5$)
Survey Area: ~1440 deg²	Comoving Survey Volume: ~150 Gpc³
T_{sys}: $100 + 120(\nu/150\,\mathrm{MHz})^{-2.55}$ K	Sensitivity after 100 hr: 50 μJy beam^{-1}

Note. Angular scales computed at 150 MHz.

established foreground filtering techniques (Pober et al. 2014; Greig & Mesinger 2015). In this section, we summarize key features of the HERA design (see Table 2) and system architecture (see Figure 15). This architecture directly inherits from the PAPER and MWA experiments. HERA begins by reusing the analog, digital, and real-time processing systems deployed for PAPER-128. This allows for immediate observing with the new elements with a well-characterized system. As HERA develops, this architecture is incrementally upgraded to improve performance and add features while simultaneously addressing issues of modularity and scalability. As with PAPER, HERA proceeds in stages of development, with annual observing campaigns driving a cycle of development, testing, system integration, calibration, and analysis. This cycle ensures that HERA's instrument is always growing, that systematics are being found and eliminated at the earliest build-out stages, that data analysis pipelines are tested and debugged while data volumes are smaller, and that HERA is always producing high quality science.

Note that in addition to the 19 elements currently observing in South Africa (and an initial prototype near Berkeley, CA), a pair of elements at the Green Bank Observatory in West Virginia have been used extensively in validation testing. Also, three elements are currently under construction at the Mullard Radio Astronomy Observatory outside Cambridge, UK for additional feed and element tests. This allows for an independent testing platform as the group at Cambridge continues to investigate both a broad-band feed, as well as ways to improve the current analog system for an improved match and noise performance.

For details of the first generation HERA system (the existing and commissioned PAPER signal path), see Parsons et al. (2010). This section will discuss the new system to be deployed
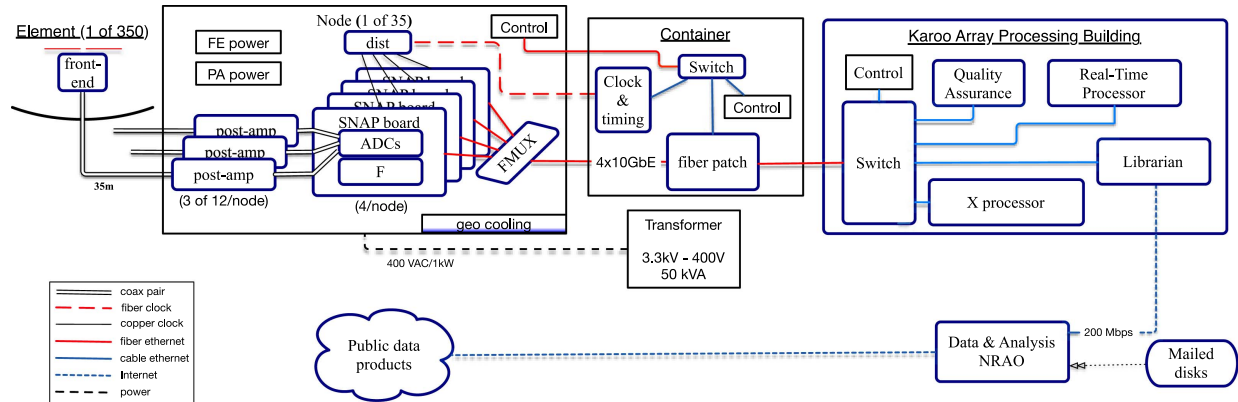
Figure 15. HERA's signal path. Front-end amplifiers at the antenna feed drive signals on short coaxial cables to field nodes. Nodes contain post-amplifiers and Smart Network ADC Processor (SNAP) boards that digitize, channelize, and packetize data for optical transmission in 10 Gb Ethernet format. Optical fibers are aggregated in a field container onto a 10 km fiber bundle connecting to the Karoo Array Processing Building, where signals are cross-multiplied in the X processor. After correlation, visibilities are stored by the Librarian, pre-processed and redundantly calibrated by the Real-Time Processor, and transmitted over the network to clusters for storage and analysis. Final products are hosted on public-facing NRAO servers, with a web interface for selecting and downloading data.
(A color version of this figure is available in the online journal.)

beginning and 2016 and tested in conjunction with the previous system. Figure 15 provides a system block diagram of the new HERA architecture.

5.1. Site

HERA is located at the Karoo Radio Astronomy Reserve, one of the two selected sites to host the SKA telescope. The Karoo Radio Astronomy Reserve was established in 2007 through the Astronomy Geographic Advantage Act in order to provide the preservation of its radio—quiet environment by restricting the use of certain radio frequencies and limiting the transmitting power in an area of $\approx$160 km radius centered at the SKA core site, near to the town of Carnavon, in the Northen Cape province. The level of protection is set to meet the requirements of the SKA project.[20] Besides offering an exceptionally good RFI environment, the Karoo site is still very accessible, making it an ideal hosting site for radio instrumentation. Beside the already mentioned HERA and SKA, it hosts the 7-element Karoo Array Telescope (KAT-7; Bernardi et al. 2016), the 64-antenna MeerKAT array (currently under construction; Booth & Jonas 2012) and the CBASS telescope (Stevenson & C-BASS Collaboration 2010). Since HERA is a scientific pathfinder for the SKA on an SKA site, it has been designated an SKA Precursor instrument.

A key element of site infrastructure is the Karoo Array Processor Building (KAPB) that hosts the storage and computing for the radio instrumentation deployed on site. In particular, the KAPB hosts the correlator for the KAT-7 and MeerKAT arrays. After correlation, the data are also archived at the KAPB and later streamed off site via fiber connection to

the Cape Town office. As discussed in Section 5.5, the KAPB also hosts the correlator and archive for HERA.

5.2. Antenna

The goals of the design principles are three-fold: (1) optimize for the delay-spectrum technique of measuring the EOR power spectrum, (2) minimize costs, and (3) design for a limited lifetime of about five years. The first item primarily means that chromatic effects corresponding to delays appropriate for the measurement described above must be below the expected signal level, which essentially determines the focal length. The second item constrains the diameter and element count, as well as the focal length over diameter ratio (f/D), based on a cost function and maximizing sensitivity per element. And the third item constrains the construction materials and methods and the operational model. This led to a fixed transit element with a diameter of 14 m to strike an optimal balance between sensitivity and systematics, as discussed previously.

The large collecting area of the HERA element yields nearly 5 times the sensitivity of an MWA tile and more than 20 times that of a PAPER element, but it does so without substantially degrading the ability to isolate and remove foreground emission on the basis of spectral smoothness. As shown in Parsons et al. (2012b) and discussed earlier, the amplitude and timescale of signal reflections relates directly to the leakage of smooth-spectrum foregrounds into regions of Fourier space used to measure reionization, as discussed in Section 3.1. To facilitate foreground filtering, HERA's antenna element is designed to suppress reflections at long time delays.

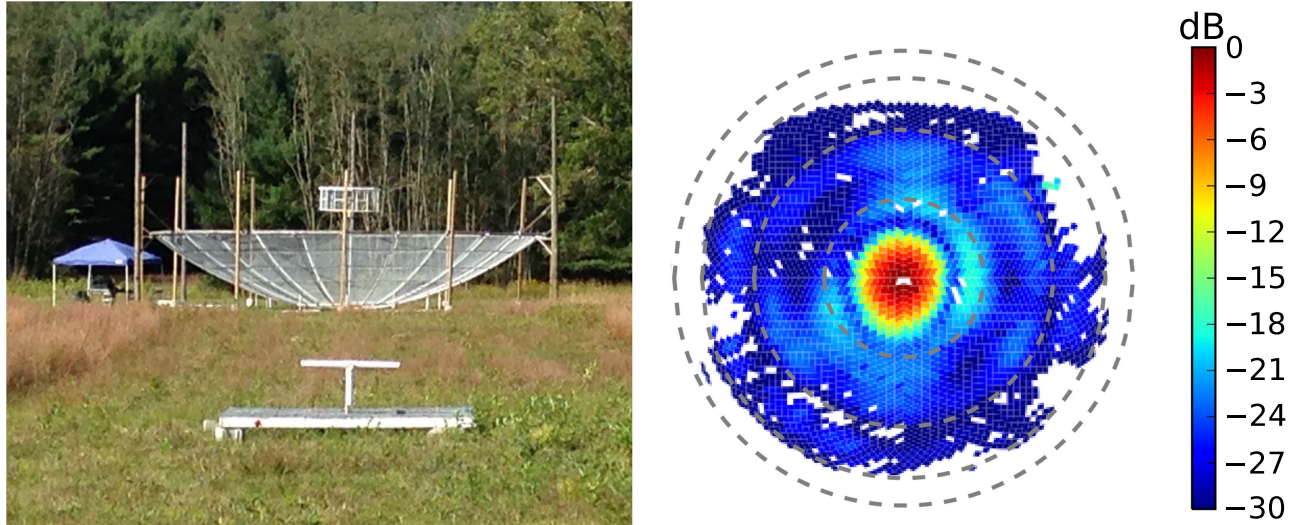Figure 16 shows the beam pattern measured at 137 MHz with a beam mapping system using the ORBCOMM satellite

---

[20] http://skatelescope.org

Figure 16. Left: the first of two prototype dishes at NRAO—Green Bank, used for measuring beam frequency structure with reflectometry and the beam pattern at 137 MHz by comparing satellite signals to the reference dipole in the foreground (Neben et al. 2016). Right: the measured EW power pattern plotted with dashed lines marking zenith angles of 20°, 40°, 60°, 80°.
(A color version of this figure is available in the online journal.)

network (Neben et al. 2016). Results indicate an effective per-element collecting area of 93 m^2, or about 60% efficiency for this version. The measured primary beam is consistent with simulations at the 0.1%–0.5% level, with a full width at half maximum of ~10°, and a first sidelobe at −20 dB (Ewall-Wice et al. 2016c; Neben et al. 2016; Patra et al. 2016, in preparation; Thyagarajan et al. 2016). Feed-to-feed coupling between the two adjacent antennas in Green Bank has been measured to be below −50 dB, providing confidence that mutual coupling will be intrinsically and algorithmically manageable. Studies of elements in a bigger array and potential screening approaches are also underway.

5.2.1. Element Construction

To minimize cost and aid in construction in a remote location, the elements are built from readily available standard construction materials, making for a very cost-effective design. The feed is supported from three utility poles using line and hardware primarily from boating activities which can handle the load and external environment. Given the close-packed design, each pole (except for the perimeter) is shared between three antennas. This both reduces the number of poles, but also makes for a balanced load. Note that the perimeter poles can be stayed with guy lines if needed. The dish rim is also supported off of these poles, each with three smaller posts in between such that the outer perimeter is regular dodecagon shape. Six of the nine intermediate posts are shared with adjacent antennas.

The center of the antenna is a cast-in-place concrete donut-shaped hub with 12 sleeves for PVC spars which provide the

support for the surface and 12 horizontal spars which allow for additional support. The twelve surface spars are made of 60 mm PVC pipe, which are stressed along three support points to approximate a parabolic shape. Note that an ideal moment-loaded beam actually attains a true parabola. The three support points (one at the hub, one about 3 m out radially and one at the rim-end) are at the correct height and angle for the underlying parabola and the PVC essentially acts as a spatial filter.

The shape between the spars is actually a parabola rather than a paraboloid, so the dish surface may more properly be called a "faceted parabola." If only twelve spars were used for the entire surface, simple Ruze losses would be quite high (about 10% at 150 MHz). Therefore, at a radius of 2.4 m another horizontal member is placed, which launches another parabolic spar leading to a Ruze loss less than 1%. Figure 17 shows this surface scheme and the panelization (left) and the offsets (in mm) of that scheme from an ideal parabola. The panel that is "left out" is the location of a door to allow access into the hub (via a small removable door and bridge). The additional intermediate spars also make the panel sizes much more manageable and better secured. The panel arrangement is also set by a standard width of mesh roll of 1.22 m.

5.2.2. Feed

The feed design is proceeding in three phases:

Phase 1: use existing PAPER dipole with new backplane and existing PAPER signal path,
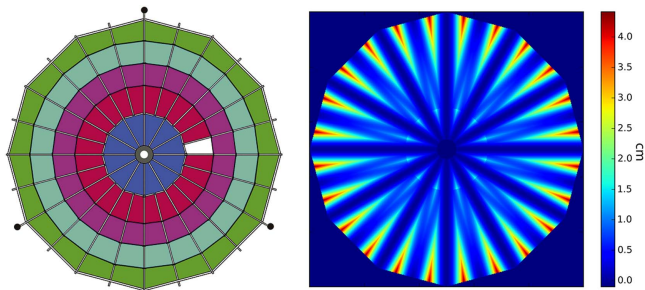*Phase 2:* updated backplane with new matching network and analog signal path,

Figure 17. Element panel plan (left) and residual from a true paraboloid (right). The white panel denotes the location of the door.
(A color version of this figure is available in the online journal.)

Phase 3: broad-band or separate low-frequency feed for full spectral coverage.

These will be discussed in turn.

Phase 1. Initially, the feed reuses the original PAPER sleeved dipole, however in a new optimized cylindrical backplane configuration. As discussed in DeBoer (2015), the optimization was based on (a) main beam efficiency, (b) cross-coupling (integrated feed pattern on the dish), (c) standing waves (blockage size), (d) frequency response and (e) polarization match. The design parameters were size of backplane, height of mast, and height of cylinder. A range of conical structures were looked at but were ruled out since it was found they introduce additional frequency structure with no real improvement in performance. The polarization figure-of-merit shown in Figure 18 is a simplified variant of the fractional power leakage as defined in Moore et al. (2016):

$$\xi = \frac{\int_{-\pi}^{\pi} [\sqrt{G(\theta, \phi = 0)} - \sqrt{G(\theta, \phi = 90)}]^2 \sin\theta d\theta}{\int_{-\pi}^{\pi} [\sqrt{G(\theta, \phi = 0)} + \sqrt{G(\theta, \phi = 90)}]^2 \sin\theta d\theta}, \quad (7)$$

where G is the beam pattern. This is basically a measurement of the beam match in the E and H planes of the antenna response. The phase 1 design process and outcome is documented in DeBoer (2015) and is currently under test on the 19 elements in South Africa. Additional studies are on-going at Green Bank and Cambridge.

This first phase design uses a 172 cm diameter backplane, with a 36 cm cylinder height. The dipole is held at 36 cm from the backplane and the back of the feed is rigged at 4.9 m above the vertex of the dish. The 10 dB input match for the feed itself spans from about 105–200 MHz. The resultant HFSS-calculated antenna performance parameters are shown in Figure 18 and beam-patterns for 110, 155, and 190 MHz are shown in Figure 19. Note that this feed differs from the earlier ORBCOMM measurements, which used a pre-optimized version.

The feed is supported by spring-tensioned aramid fiber lines from the three poles via a rigid support to which the feed cage and dipole attach. The tensioning line goes down centrally to the hub to hold the feed rigidly in place at the correct height. This also stabilizes the feed in position and allows for strain relief on the coaxial cables.

The low noise amplifier/balun integrates directly to the base of the feed dipole in the same configuration as per PAPER. The 150 m length of 75 Ω cable used in the initial design also runs down centrally and then over to the post-amplifier module (PAM), which is housed near the RFI-shielded container containing the digital electronics.

Phase 2. This phase replaces the extant PAPER signal path with new front-end and PAMs, discussed in Section 5.4. Depending on the status of feed optimization and development the current feed backplane or the feed itself may be swapped out with new designs. The new system incorporates the node-based system, with short analog cables and field-deployed digitizers (Section 5.5).

Phase 3. A wideband feed is being designed for the next phase of HERA (see e.g., Figure 20). This feed will have wider bandwidth (50–250 MHz) and have comparable (or better) performance across the EOR band; if not the deployment will be after EOR observations. This wider band will open the window of Cosmic Dawn and the latest stages of the Epoch of Re-ionization to HERA. Observations at frequencies above 200 MHz can also provide a consistency check for lower frequency measurements, as the maximum brightness of the 21 cm signal at late times can be constrained with other probes (Pober et al. 2014). The feed version shown is based on a modified TEM horn concept where the feed's beam is optimized for the appropriate illumination of the HERA dish to maximize sensitivity. This is to maximize the effective aperture while minimizing the system temperature (receiver noise, ohmic losses, spill-over, etc.). The new feed will replace the current PAPER dipoles and will therefore be mechanically compatible with the current dishes being deployed in South Africa.

Furthermore, as shown in de Lera Acedo et al. (2015), room temperature ultra low receiver noise (<35 K including matching noise) above 100 MHz can be achieved with COTS transistors if a proper feeding mechanism and matching are designed. Despite the fact that sky noise is dominant for most of the EoR band, good matching is always critical in wide band systems, and specifically in the HERA case it is important to ensure good power match as well as noise match in order to reduce the effects of unwanted reflections (Fagnoni & de Lera Acedo 2016). We envisage having such a feeding mechanism in the new feed where the first stage LNA will be connected directly to the feeding point of the feed antenna.

Additionally, we are analyzing the effect of coupling with numerical simulations where we can quantify and understand the effects of mutual coupling, which so far only looks
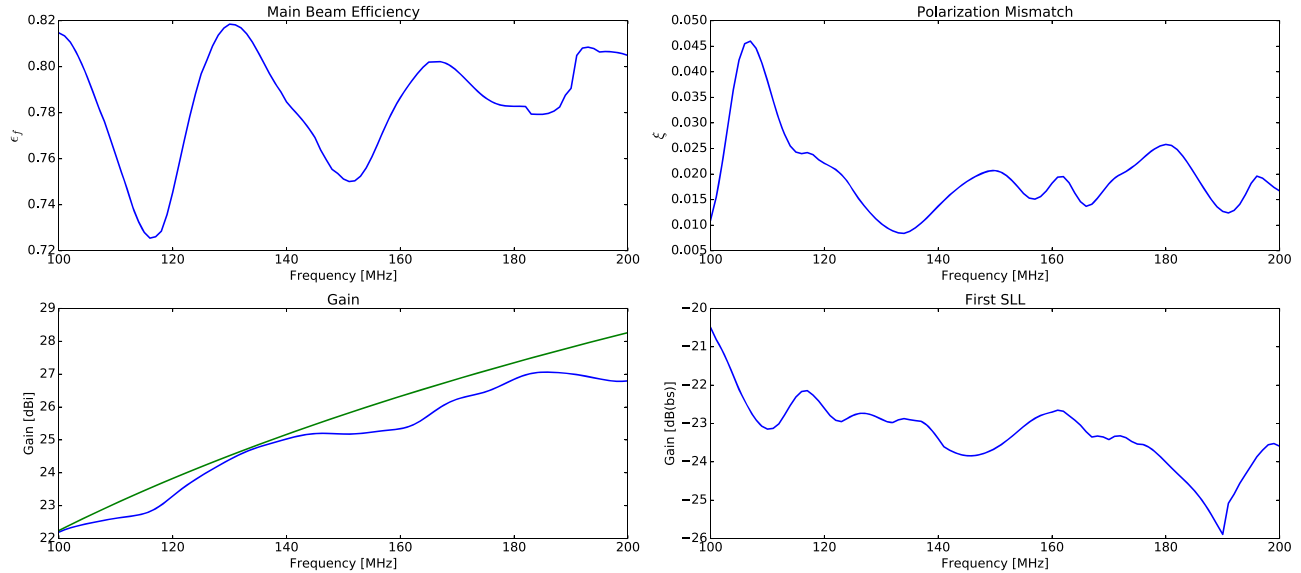
Figure 18. Antenna parameters from the feed optimization analysis. All calculations were done using HFSS on the final design as described. Upper left: fraction of feed power illuminating the primary (main beam efficiency). Upper right: polarization mismatch as defined in Equation (7). Lower left: total gain (blue) contrasted with a fixed efficiency of 78%. Lower right: first side-lobe level relative to the main beam peak.
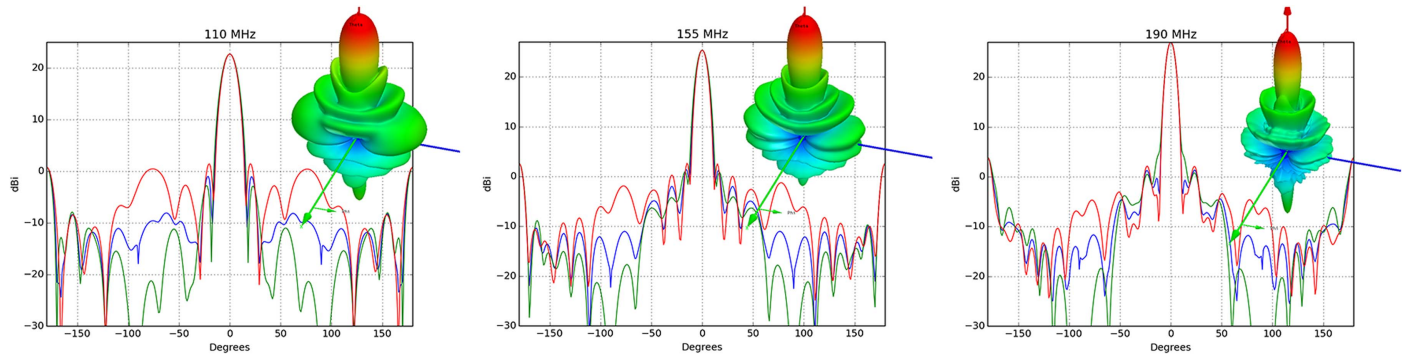(A color version of this figure is available in the online journal.)

Figure 19. Antenna patterns at 110, 155 and 190 MHz calculated with HFSS and the adopted design. Red curves are E-plane, green are H-plane at blue at 45°. Inset is the full 3D pattern.
(A color version of this figure is available in the online journal.)

substantial in the far out side-lobes. This will allow us to optimize the feed design for reduced coupling as well as evaluate the need of "skirts" for cross-coupling reduction or other further dish optimizations. This work will benefit from the existence of several prototype systems including the three-dish HERA system near Cambridge.

5.3. Array Configuration

As a focused experiment, HERA's configuration is optimized for the robust foreground-avoidance approach to EoR power spectrum estimation. This requires a densely packed core of antenna elements, maximizing sensitivity to short baselines—those least contaminated by foreground chromaticity (i.e., the wedge). Furthermore, the configuration should be highly redundant, both to increase sensitivity for the delay-spectrum strategy of PAPER (Parsons et al. 2012a) and provide for redundant baseline calibration (Liu et al. 2010; Zheng et al. 2014). On the other hand, it is also desirable to improve the mapmaking ability of the array for calibration and map-based power spectrum estimation with longer baselines and a densely sampled *uv*-plane (Dillon et al. 2015b). This tradeoff was closely examined by Dillon & Parsons (2016) and the HERA configuration was drawn from one of the designs considered therein.
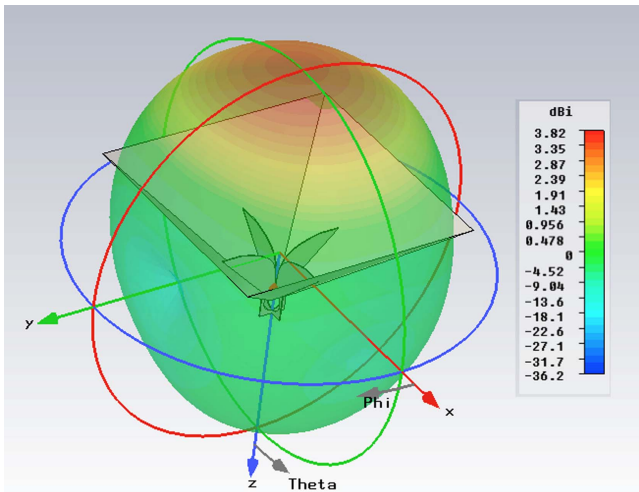
Figure 20. Future potential HERA feed showing its directive beam pointed toward the dish. It is based on a modified ridge TEM horn and is currently under investigation at Cambridge University.

(A color version of this figure is available in the online journal.)

HERA's 320 core elements are arranged in a compact hexagonal grid, split into three displaced segments to cover the uv-plane with sub-aperture sampling density (see Figure 21). Splitting the core into three sections triples the density of instantaneous sampling of the uv-plane, improving HERA's mapmaking ability. Furthermore, the core is supplemented by 30 additional outrigger elements to tile the uv-plane with instantaneously complete sub-aperture sampling out to 250λ and complete aperture-scale sampling out to 350λ (at 150 MHz). This sub-aperture sampling strategy suppresses grating lobes in the instrument's point-spread function and provides information for calibrating and correcting direction-dependent antenna responses (Dillon & Parsons 2016). Even with the sub-aperture dithering and long baselines, the design is sufficiently redundant to take advantage of redundant baseline calibration technique and robust to the failure of individual elements. Resulting calibration errors range from ~5% (in the core) to ~10% (for outriggers) of the residual fractional noise per antenna after averaging. The split core increases the gain errors on the core elements by only ~0.1% from a solid hexagonal configuration. HERA's compact and redundant design allows it to fully utilize PAPER's robust approach to calibration and foreground mitigation, but it also provides for excellent imaging capability that can be leveraged to suppress foregrounds and improve access to the 21 cm reionization signal.

5.4. Analog Signal Path

HERA's analog signal path from 50–250 MHz with the full performance EOR band of 100–200 MHz, as shown in Figure 2

and discussed in Section 4.2, emphasizes spectral smoothness and robustness. Although the low-frequency sky has an intrinsically bright signal level, in the desired "cold patches" the sky temperature is only about 30 K at the upper frequency end, so relatively low receiver temperatures are desired. Note that at the low end of the band (50 MHz), the sky temperature is greater than 1000 K and across the EOR band it ranges from about 100–400 K. With receiver temperatures of 30–100 K readily achievable with ambient temperature electronics however HERA's low-noise amplifiers (LNAs) may be inexpensive, passively cooled components integrated into the antenna feed.

As part of the delay specification, HERA's signal path emphasizes careful impedance matching between each component to minimize signal reflections that can worsen foreground leakage for the delays of interest. This means that the emphasis is to reduce the delay-value of a reflection, which allows for a design degree of freedom. One such design element is to house the analog-to-digital converters (ADCs) in "nodes" near the antenna elements to limit the total analog path length. This length is set to be 35 m, such that the round-trip delay corresponds to about $0.15\,h\,\mathrm{Mpc}^{-1}$, which remains in the wavenumbers near the wedge. The project is also examining the impact of having a range of varying analog path lengths.

The Phase 2/3 analog signal path comprises the front-end module (FEM) at the feed, the PAM at field-deployed nodes, and the ~35 m coaxial cable in between. Also included are the monitor and control aspects to control and measure its state.

Front-End Module (FEM). The FEM consists of an LNA as the very first stage in the chain for each polarization. This component for the existing feed design will be a differential low noise amplifier which consists of two sets of LNAs feeding each dipole arm followed by a balun (or hybrid coupler). The output from this point is then all single ended and mostly matched to 50 Ω impedance, excepted as needed to drive the Phase 1 75 Ω cables. While it is desirable to be sky noise dominated in the HERA band, meaning for the first stage, the best achievable noise match must be obtained, it must not come at a too great cost to the power match since reducing the ripple across the band is absolutely essential. This trade-off will be observed carefully to ensure the FEM is both low-noise and well-matched. This stage is followed by carefully matched filters and further amplifications of the signal. In order to ensure very low reflection on the line a large matching attenuator will be used at each end of the cable after the bias-Tee circuit.

The FEM will also include a number of useful signal conditioning operations. One of these will be to have a phase switch for each polarization as early as possible in the signal chain. The switch will offer very low phase imbalance and will be controlled by differential lines. The Walsh functions (orthogonal phase switching signals) will be generated in the SNAP board (Section 5.5) and used to control FEMs in the field.
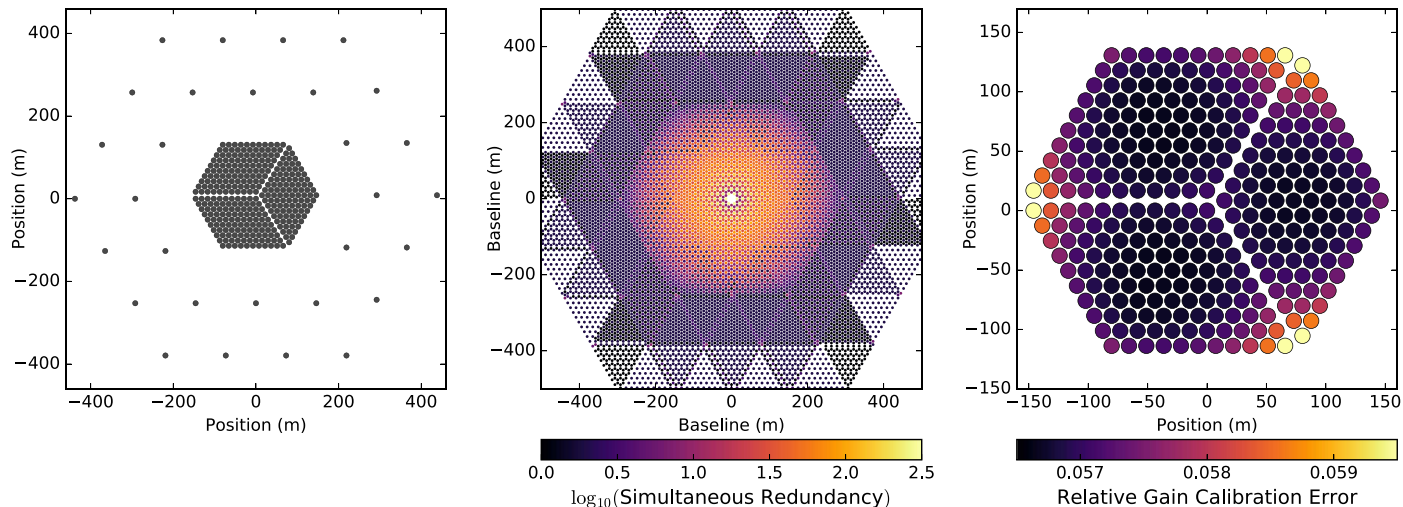
Figure 21. HERA's elements are divided between a 320-element, hexagonally packed core and 30 outriggers (left). This produces instantaneous *uv* coverage at triple the element packing out to 250λ at 150 MHz, supressing grating lobes in the synthesized beam (middle). All 350 elements can be redundantly calibrated using the Liu et al. (2010) technique, yielding calibration errors that are a small fraction of the residual noise per antenna (right). See Dillon & Parsons (2016) for discussion. (A color version of this figure is available in the online journal.)

Another useful feature of the FEM will be an integrated "Dicke" switching radiometer similar to the EDGES experiment (Rogers & Bowman 2012). The circuit provides the capability of switching between the output of the antenna, a calibrated noise source and a 50 Ω ambient load. The antenna measures only a fraction of the sky brightness temperature, determined by the matching between the antenna and receiver. Three spectrometer measurements (antenna, ambient load and noise source) as well as additional lab measurements of its microwave performance and noise-parameters of the FEM prior to deployment then allow good calibration of the output spectrum. An on-board temperature sensor near the noise source will also aid with the calibration of the receiver chain. The FEM will be housed in a rugged $5 \times 5 \times 10$ cm unit which is water and dust resistant.

Post-Amplifier Module (PAM). The PAMs consists of further amplification and filtering of the RF signals received from the FEMs. They are designed to provide the anti-aliasing filtering (DC–250 MHz) prior to the ADCs on the SNAP board. These modules also feed the DC voltage supply to the FEMs on the antennas and relay the control and monitoring signals using a 1-Wire interface. Each PAM will provides a controllable digital attenuator to allow the input levels into the ADC to be set. All the controllable circuits such as RF switches and attenuators will have a unique address. It is envisaged that most of the lower level control signals which are not data critical will be achieved though the node computer. The phase switch, however, is a data critical control signal sent directly by the SNAP boards. Each PAM will be rack mountable (3U, 5HP) and will control a single antenna containing two polarizations.

5.5. Digital Signal Path

Although in the past, correlator development has been one of the most expensive and complex aspects of building a large array or radio interferometers, this is no longer generally the case. The Collaboration for Astronomy Signal Processing and Electronics Research (CASPER; Parsons et al. 2006, casper. berkeley.edu) is a community of astronomers and engineers who work to reduce the cost and complexity of radio astronomy signal processing systems through the development of open-source, general-purpose hardware and software. CASPER currently has several hundred members at 73 institutions, and has developed six generations of FPGA-based signal processing hardware, shown in Figure 22. PAPER has applied CASPER technology to develop and deploy new correlators annually for five years running, each quadrupling the computational capacity of its predecessor. Key to the upgradability of the PAPER correlator is the use of modular processing engines, and industry-standard digital interconnect based on off-the-shelf Ethernet switches (Parsons et al. 2008) to perform the antenna/frequency data transpose required by FX correlators.

HERA will maintain both PAPER's well-proven digital system architecture along with the simple scheme of real-sampling and channelizing the entire analog passband at once. However, in order to meet the 35 m specification for maximum analog signal path length, as well as ensure future scalability of the system, HERA-350 will adopt an architecture of field-deployed amplification, digitization, and channelization nodes, building on MWA and Allen Telescope Array (Welch et al. 2009) heritage. Digital data streams from multiple nodes will
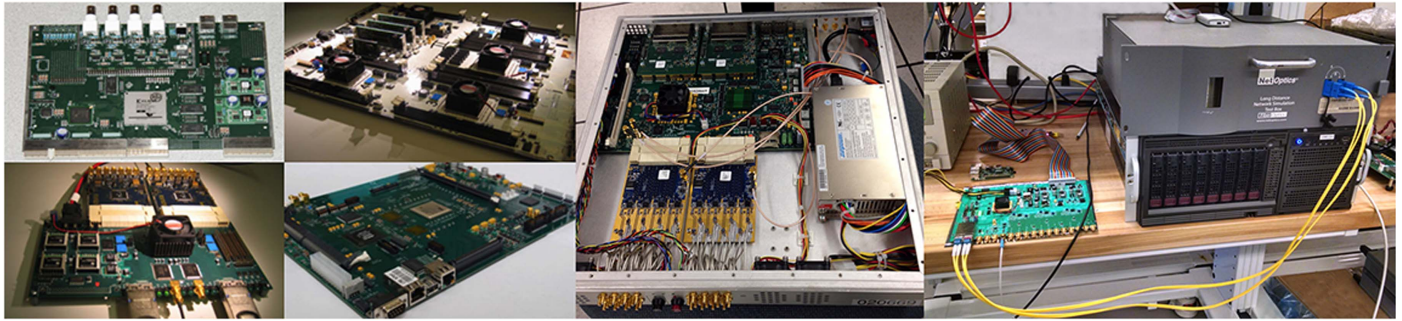
Figure 22. Six generations of CASPER digital signal processing (left to right) culminating in the SNAP board (right, along with the long-haul fiber-link test setup). By preserving its design tools, signal processing libraries, and interface code between hardware generations, CASPER hardware and a modular architecture have enabled the PAPER correlator to be easily upgraded for HERA (Parsons et al. 2006, 2008).
(A color version of this figure is available in the online journal.)

converge to a container adjacent to the HERA array, from which they will be routed to a central processor building where correlation and further processing will take place. This section will step through the digital signal path, shown in Figure 15, organized by location: node, container, and processing building.

Node. HERA-350 employs RFI-tight node enclosures that each contain the final gain (PAM) and digitization stages for signals from 12 antennas, along with power supplies, cooling, sensors, and a small server for monitor/control. This has led to the development of a new CASPER platform based around a Xilinx Kintex 7 FPGA, which incorporates on-board ADCs: the Smart Networked Analog-Digital Processor (SNAP[21], shown in Figure 22). SNAP is an inexpensive and flexible "Analog in, 10 GbE out" device which uses a pair of industry-standard SFP+ modules for output over either copper or optical fiber cables. Co-designed by UC Berkeley and NRAO, the SNAP board will serve as both the digitizer and F-engine in HERA's FX correlator architecture. Each SNAP board digitizes and channelizes a 0–250 MHz band for 6 input signals (3 antennas, dual-polarization), with a complete node containing 4 SNAP boards.

Following digitization and channelization, a ∼200 MHz band of runtime-selectable channels is output as a UDP stream over optical fiber. Coarse Wavelength Division Multiplexing (CWDM) technology allows the 10 Gb s^{-1} Ethernet streams from the four SNAP boards in a node to share a single fiber, which is routed to a central container, and on to the correlator. In this configuration, the fiber from each node is input directly into an Ethernet switch using a single QSFP+ 40GBASE-LR4 transceiver, which provides built-in multiplexing and demultiplexing capabilities and may be operated as 4 independent transceivers. Laboratory tests have successfully demonstrated robust transmission from the SNAP board through CWDM

multiplexers and 10 km single mode fiber optic cable, into a 10 GbE switch using inexpensive, commercially available optical transceivers (see far right of Figure 22).

While some applications may utilise SNAPs in multiple-board chassis, for HERA SNAP is housed in a field-deployable RFI-tight box. The node enclosure itself is an RFI-tight housing that can handle the signal paths for up to 12 antennas. The enclosures are placed throughout the array to minimize the total number constrained by the 35 m maximum cable length. For outrigger antennas the delay specification is not critical, so the cable-length to those may be as long as practical. In total, including outriggers, the HERA-350 design demands 34 nodes, or an average of just over 10 antennas/node.

The node uses forced-air, Earth-coupled cooling similar to that implemented for the Allen Telescope Array (Welch et al. 2009). An AC-synchronous motor continually blows air through 30 m of underground 150 mm PVC pipe, which vents through the enclosure from bottom to top. The underground pipe is at least 1 m deep, so that the emerging air is very thermally stable on seasonal time constants. The PAM is the lowest component since it is the most sensitive and also generates the least heat. SNAP boards, monitor and control hardware, and power supplies will be positioned above the PAMs. Remote monitoring capabilities will include node temperature, air-flow and power, with remote control of power to the node's various active components.

Support Container. HERA's support container houses two significant subsystems adjacent to the array. The first is a timing subsystem that maintains a GPS-disciplined oscillator and distributes timing signals to the nodes. These signals comprise a sampling clock (or other frequency reference from which the sampling clock may be derived) and 1 pulse-per-second (PPS) synchronization pulses. The timing subsystem will distribute clock and synchronization signals over fiber and, depending on cost and performance, will utilize either

---

[21] https://casper.berkeley.edu/wiki/SNAP

industry-standard distribution solutions, or the White Rabbit protocol (Moreira et al. 2009).

The second subsystem is a passive fiber optic patch panel that couples the optical network from the nodes into the 192-filament optical fiber bundle that is routed to the Karoo Array Processing Building.

HERA and the KAPB. Approximately 10 km (by fiber path) from the array support container is the Karoo Array Processor Building (KAPB), the purpose-built facility to house radio astronomy computing resources in the remote desert introduced in Section 5.1. A fiber optic bundle from the HERA container enters the KAPB and is patched into local fiber cables, which terminate in QSFP+ optical transceivers. These QSFP+ transceivers are input to a 64-port QSFP+ 10/40 GbEthernet switch—such devices are readily available on the commercial market today, at relatively low cost. The Ethernet switch forms the core of the HERA correlator's data interconnect, and provides the antenna-frequency data transpose which allows cross-multiplication of antenna signals to be easily parallelized by frequency over many compute nodes performing cross-multiplication ("X-Engines").

These compute nodes are anticipated to be 30×86 servers, each hosting a pair of Nvidia Graphics Processing Units (GPUs) and two dual 10GbE network interface cards. This estimate assumes an identical configuration to the current PAPER X-Engine hardware, and conservatively assumes that the computational capacity of GPU accelerator cards will double once prior to purchasing these servers. No improvement in data transfer speed from CPU to host is assumed.

Other X-Engine realizations are under active evaluation, including a solution involving AMD GPUs and the highly optimized cross-multiplication kernels developed for the CHIME Pathfinder array (Denman et al. 2015), and FPGA-based implementations involving both CASPER, and commercially available, platforms.

Output data from the correlator are written to the data storage system described in the following section.

5.6. Data Processing and Management

The HERA correlator generates ~4 TB of raw data per 12 hr observing day. These data are transferred to an on-site cluster (the Real Time Processor, RTP) where they are calibrated on the basis of redundancy (Zheng et al. 2014) and averaged in time and frequency to the limit possible without information loss. Raw products are archived in an on-site 1.5 PB storage array; reduced size products are transferred via the internet to the NRAO Data Archive. The RTP supports multiple data volume reduction schemes including delay-delay-rate filtering (Parsons et al. 2014), sub-array selection, and baseline dependent averaging. The data cataloging system, known as the "librarian" catalogs files, coordinates data transfers, and
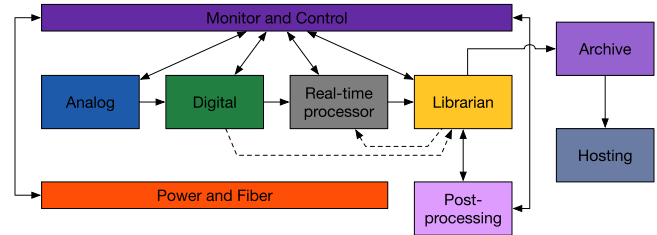

Figure 23. High-level architecture.
(A color version of this figure is available in the online journal.)

cross-references data to observation meta-data. The high-level architecture is shown in Figure 23.

NRAO will host the archiving of HERA calibration products and images within the existing NRAO EVLA Next Generation Archive System (NGAS) at the Domenici Science Operations Center (DSOC). The NGAS software provides indexing via instrument defined keywords and supports public and private retrieval of both raw and processed products via web based searches with access controlled by the NRAO user database.

Routine data inspection and lightweight analysis tasks is performed on a processing cluster within the DSOC and includes access to a 1 PB high speed Lustre filesystem. For bulk application of processing-intensive data pipelines to HERA data NRAO manages the distribution of load between the in house cluster, NSF funded XSEDE resources (www.xsede.com) and if necessary costed access to Amazon Web Services (AWS) cloud computing via AWS's spot market (aws.amazon.com/ec2/spot)

5.7. Analysis Pipelines

HERA builds on the rich legacy of PAPER and MWA software and database systems developed for field operations, data analysis, and simulation. Examples range from the strictly versioned and unit-tested packages for field-deployed systems (e.g., the correlator, real-time processing, and monitor/control systems) to loose collections of scripts written for exploratory analysis. Software packages that support HERA analysis are open source, publicly hosted[22], revision controlled, and unit-tested. These include OMNICAL, a complete package for redundant baseline calibration; Astronomical Interferometry in Python (AIPY), a set of tools and file-format interfaces for reading visibilities, calibrating, rephasing, imaging, and deconvolution; Fast Holographic Deconvolution (FHD), a purpose-built tool for imaging, calibration, and foreground forward-modeling and subtraction (Sullivan et al. 2012); Precision Radio Interferometry Simulator (PRISim), a package

---

[22] Including   github.com/AaronParsons/aipy,   github.com/JeffZhen/omnical, github.com/MiguelFMorales/FHD, github.com/MiguelFMorales/eppsilon, github.com/jpober/21cmSense, github.com/nithyanandan/PRISim, and https://github.com/BradGreig/21CMMC.

for accurately simulating wide-field interferometric observations; 21cmFAST (Mesinger et al. 2011), a fast, semi-numerical 21 cm signal simulator, and 21cmSense (Pober et al. 2014), a tool for forecasting power spectrum sensitivity. Other project code is aggregated and revision controlled in a public repository with separate sandboxes for each developer to ensure that HERA members have up-to-date copies of all project code to facilitate sharing and debugging. Such code includes the PAPER pipeline for foreground filtering and estimating power spectra from visibility data, the MWA power spectrum analysis codes—εppsilon (B. J. Hazelton et al. 2016, in preparation) and the empirical covariance technique of Dillon et al. (2015a)—as well as machine-learning-based source finding, verification, and removal tools (Carroll et al. 2016; A. P. Beardsley et al. 2016, in preparation; Jacobs et al. 2016).

New software development is focusing on integrating and improving the MWA and PAPER power spectrum and foreground removal pipelines, developing a monitor and control software interface and database for recording instrument metadata, extending, with support from Scuola Normale Superiore, semi-analytic and numerical models of the 21 cm signal for robust parameter estimation, and developing machine learning interpolations of simulations for joint Monte Carlo estimation of cosmological and astrophysical parameters.

6. Schedule and Status

On-site construction is proceeding in stages, starting from the initial 19 elements currently in place. Elements 20–37 are currently under construction, to be completed in 2016. These will be used in conjunction with the thoroughly characterized extant PAPER signal path and processing hardware for a very low risk initiation of scientific observations. As elements 38 to 128 are installed in 2017, they can immediately be placed within the array and be used for observing.

During this period, infrastructure for the new node-based system will be installed and tested with the first elements beyond 128. After the HERA-128 observing season, the full array will be transitioned to use HERA's new hardware infrastructure. In this same time frame, the existing PAPER processing container will be moved to the edge of the array to house the timing sub-system and fiber optic splice cabinet while the correlator will move to the KAPB. The overall plan is shown in Figure 24.

The optimal EoR observing window is from September to April, with power spectrum limit results appearing about one year later. Concurrent technique development and deployment will be on-going. A breakdown of activities is shown below.

2016/17: Observe with H37. Real-time data pipeline, delay-space power spectrum (DSPS) pipeline, FHD pipeline. 21 cm framework for incorporating with other probes. Construct H128.
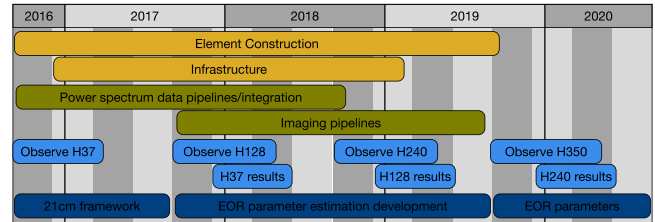

Figure 24. Timeline of HERA construction, analysis development, observation, and scientific output. Activities after 2016 are contingent upon funding. (A color version of this figure is available in the online journal.)

2017/18: Observe with H128. Real-time calibration pipeline. DSPS/FHD/global sky model integration. Snapshot imaging pipeline. EoR parameter estimation development. H37 results. Construct H240. Data products: power spectrum, Stokes I maps.

2018/19: Observe with H240. Foreground-filtered imaging pipeline. EoR parameter estimation development. H128 results. Construct H350. Data products: power spectrum, Stokes IQUV maps, foreground image cube.

2019/20: Observe with H350. EOR parameter estimates. H240 results. Data products: power spectrum, global sky model IQUV, snapshots, foreground-filtered image cube.

2020+: Observe with H350. H350 results. Data products: power spectrum, global sky model IQUV, snapshots, foreground-filtered image cube.

7. Conclusion

The first generation instruments are beginning to provide constraints on some models of the reionization of the universe, as well as developing the key algorithms and comprehension to enable detection of the power spectrum of the EOR. In the past three years, we have developed the EoR window paradigm for isolating foreground systematics, implemented novel calibration and power spectrum analysis pipelines, made precision measurements of astrophysical foregrounds, and published deep power spectrum limits that constrain heating in the early universe. However, as shown in Figures 4 and 5 and Table 1, using proven methods these instruments are not likely to make a robust detection or enable its characterization as a function of redshift or astrophysical parameters. We have drawn from this development to design and develop a purpose-built array to detect (or, if current arrays succeed, provide a robust confirmation of) the signature of the power spectrum of the EOR. Since it is designed for a specific experiment, HERA's optimization allows for a substantial increase in sensitivity to enable precise constraints of EOR astrophysics and a broad range of high-impact secondary science.

HERA will use the delay-spectrum approach to detect and characterize the EOR across its full redshift range at spatial scales that inform cosmology and astrophysics in the early universe. The first 19 elements are on the ground and being used with extant components from PAPER, and construction has begun on another 18 to bring the array to 37 elements. With 37 elements, HERA should have sufficient sensitivity to detect the peak of reionization at wavenumbers greater than $0.15\,h\mathrm{Mpc}^{-1}$ with a season's worth of observing. Building out to the full 350 elements should enable HERA to fully characterize the EOR power spectrum and potentially begin to directly image this epoch over a portion of the sky. These results are a necessary component to enable future arrays like the Square Kilometer Array (SKA; e.g., Mellema et al. 2013; Greig et al. 2015) to do detailed mapping of structures over the entire sky.

References

Aguirre, J. E., Kohn, S. A., Zachary, M., & Washington, I. Q. 2016, ApJ, submitted
Ahn, K., Iliev, I. T., Shapiro, P. R., et al. 2012, ApJL, 756, L16
Ali, S. S., Bharadwaj, S., & Chengalur, J. N. 2008, MNRAS, 385, 2166
Ali, Z. S., Parsons, A. R., Zheng, H., et al. 2015, ApJ, 809, 61
Allison, R., Caucal, P., Calabrese, E., Dunkley, J., & Louis, T. 2015, PhRvD, 92, 123535
Asad, K. M. B., Koopmans, L. V. E., Jelić, V., et al. 2015, MNRAS, 451, 3709
Barry, N., Hazelton, B., Sullivan, I., Morales, M. F., & Pober, J. C. 2016, MNRAS, 461, 3135
Beardsley, A. P., Hazelton, B. J., Sullivan, I. S., et al. 2016, ApJ, 833, 102
Bernardi, G., de Bruyn, A. G., Brentjens, M. A., et al. 2009, A&A, 500, 965
Bernardi, G., de Bruyn, A. G., Harker, G., et al. 2010, A&A, 522, A67
Bernardi, G., Greenhill, L. J., Mitchell, D. A., et al. 2013, ApJ, 771, 105
Bernardi, G., Venturi, T., Cassano, R., et al. 2016, MNRAS, 456, 1259
Bolton, J. S., Haehnelt, M. G., Warren, S. J., et al. 2011, MNRAS, 416, L70
Booth, R. S., & Jonas, J. L. 2012, AfrSk, 16, 101
Bosman, S. E. I., & Becker, G. D. 2015, MNRAS, 452, 1105
Bouwens, R. J., Illingworth, G. D., Oesch, P. A., et al. 2015a, ApJ, 811, 140
Bouwens, R. J., Illingworth, G. D., Oesch, P. A., et al. 2015b, ApJ, 803, 34
Bowman, J. D., & Rogers, A. E. E. 2010, Natur, 468, 796
Bowman, J. D., Cairns, I., Kaplan, D. L., et al. 2013, PASA, 30, 31
Carilli, C. L., & Sims, P. 2016, HERA Imaging: Mock Observations using CASA, Memo Series 12, HERA Collaboration
Carilli, C. L., Wang, R., Fan, X., et al. 2010, ApJ, 714, 834
Carroll, P. A., Line, J., Morales, M. F., et al. 2016, MNRAS, 461, 4151
Dalal, N., Pen, U.-L., & Seljak, U. 2010, JCAP, 11, 7

Datta, A., Bowman, J. D., & Carilli, C. L. 2010, ApJ, 724, 526
de Lera Acedo, E., Razavi-Ghods, N., Troop, N., Drought, N., & Faulkner, A. J. 2015, ExA, 39, 567
de Oliveira-Costa, A., Tegmark, M., Gaensler, B. M., et al. 2008, MNRAS, 388, 247
DeBoer, D. R. 2015, HERA Phase I Feed, HERA Memo 11, HERA Collaboration
DeBoer, D. R., & Parsons, A. R. 2015, Configuration of the HERA Element, HERA Memo 5, HERA Collaboration
Denman, N., Amiri, M., Bandura, K., et al. 2015, in 2015 IEEE 26th Int. Conf. on Application-specific Systems, Architectures and Processors (ASAP), 35
Dijkstra, M., Wyithe, S., Haiman, Z., Mesinger, A., & Pentericci, L. 2014, MNRAS, 440, 3309
Dillon, J. S., Liu, A., & Tegmark, M. 2013, PhRvD, 87, 043005
Dillon, J. S., & Parsons, A. R. 2016, ApJ, 826, 181
Dillon, J. S., Liu, A., Williams, C. L., et al. 2014, PhRvD, 89, 023002
Dillon, J. S., Neben, A. R., Hewitt, J. N., et al. 2015a, PhRvD, 91, 123011
Dillon, J. S., Tegmark, M., Liu, A., et al. 2015b, PhRvD, 91, 023002
Doré, O., Bock, J., Ashby, M., et al. 2014, arXiv:1412.4872
Ellingson, S. W., Clarke, T. E., Cohen, A., et al. 2009, IEEEP, 97, 1421
Evoli, C., Mesinger, A., & Ferrara, A. 2014, JCAP, 11, 024
Ewall-Wice, A., Hewitt, J., Mesinger, A., et al. 2016a, MNRAS, 458, 2710
Ewall-Wice, A., Dillon, J. S., Hewitt, J. N., et al. 2016b, MNRAS, 460, 4320
Ewall-Wice, A., Bradley, R., Deboer, D., et al. 2016c, ApJ, 831, 196
Fagnoni, N., & de Lera Acedo, E. 2016, in ICEAA Conf., The Hydrogen Epoch of Reionization Array (HERA)—Improvement of the Antenna Response with a Matching Network and Scientific Impacts
Fan, X., Strauss, M. A., Becker, R. H., et al. 2006, AJ, 132, 117
Fialkov, A., Barkana, R., Tseliakhovich, D., & Hirata, C. M. 2012, MNRAS, 424, 1335
Fialkov, A., & Loeb, A. 2016, ApJ, 821, 59
Fontana, A., Vanzella, E., Pentericci, L., et al. 2010, ApJL, 725, L205
Furlanetto, S. R. 2006, MNRAS, 371, 867
Furlanetto, S. R., Zaldarriaga, M., & Hernquist, L. 2004, ApJ, 613, 1
Greig, B., & Mesinger, A. 2015, MNRAS, 449, 4246
Greig, B., Mesinger, A., & Koopmans, L. V. E. 2015, arXiv:1509.03312
Haiman, Z., & Holder, G. P. 2003, ApJ, 595, 1
Hazelton, B. J., Morales, M. F., & Sullivan, I. S. 2013, ApJ, 770, 156
Iliev, I. T., Mellema, G., Shapiro, P. R., & Pen, U.-L. 2007, MNRAS, 376, 534
Iliev, I. T., Mellema, G., Shapiro, P. R., et al. 2012, MNRAS, 423, 2222
Jacobs, D. C., Hazelton, B. J., Trott, C. M., et al. 2016, ApJ, 825, 114
Jelić, V., Zaroubi, S., Labropoulos, P., et al. 2008, MNRAS, 389, 1319
Kassim, N. E., Clarke, T. E., Hicks, B., et al. 2013, in American Astronomical Society Meeting Abstracts 221, 328.04
Kohn, S. A., Aguirre, J. E., Nunhokee, C. D., et al. 2016, ApJ, 823, 88
Lidz, A., Zahn, O., Furlanetto, S. R., et al. 2009, ApJ, 690, 252
Liu, A., & Parsons, A. R. 2016, MNRAS, 457, 1864
Liu, A., Parsons, A. R., & Trott, C. M. 2014a, PhRvD, 90, 023018
Liu, A., Parsons, A. R., & Trott, C. M. 2014b, PhRvD, 90, 023019
Liu, A., Pritchard, J. R., Allison, R., et al. 2016, Phys. Rev. D, 93, 043013
Liu, A., & Tegmark, M. 2011, PhRvD, 83, 103006
Liu, A., Tegmark, M., Morrison, S., Lutomirski, A., & Zaldarriaga, M. 2010, MNRAS, 408, 1029
Lorimer, D. R., Bailes, M., McLaughlin, M. A., Narkevic, D. J., & Crawford, F. 2007, Sci, 318, 777
Malloy, M., & Lidz, A. 2013, ApJ, 767, 68
Manzotti, A., Dodelson, S., & Park, Y. 2016, PhRvD, 93, 063009
Masui, K., Lin, H.-H., Sievers, J., et al. 2015, Natur, 528, 523
McGreer, I. D., Mesinger, A., & D'Odorico, V. 2015, MNRAS, 447, 499
McLeod, D. J., McLure, R. J., Dunlop, J. S., et al. 2015, MNRAS, 450, 3032
McQuinn, M., Hernquist, L., Zaldarriaga, M., & Dutta, S. 2007, MNRAS, 381, 75
Mellema, G., Koopmans, L. V. E., Abdalla, F. A., et al. 2013, ExA, 36, 235
Mesinger, A., Aykutalp, A., Vanzella, E., et al. 2015, MNRAS, 446, 566
Mesinger, A., Ferrara, A., & Spiegel, D. S. 2013, MNRAS, 431, 621
Mesinger, A., Furlanetto, S., & Cen, R. 2011, MNRAS, 411, 955
Mesinger, A., McQuinn, M., & Spergel, D. N. 2012, MNRAS, 422, 1403
Moore, D., Aguirre, J. E., Parsons, A., et al. 2016, Astrophysical Journal, submitted arXiv:1502.05072

Moore, D. F., Aguirre, J. E., Parsons, A. R., Jacobs, D. C., & Pober, J. C. 2013, ApJ, 769, 154

Morales, M. F., Hazelton, B., Sullivan, I., & Beardsley, A. 2012, ApJ, 752, 137

Moreira, P., Serrano, J., Wlostowski, T., Loschmidt, P., & Gaderer, G. 2009, in 2009 Int. Symp. on Precision Clock Synchronization for Measurement, Control and Communication, 1

Mortlock, D. J., Warren, S. J., Venemans, B. P., et al. 2011, Natur, 474, 616

Mortonson, M. J., & Hu, W. 2008, ApJ, 672, 737

National Academy of Science 2010, New Worlds, New Horizons in Astronomy and Astrophysics http://sites.nationalacademies.org/bpa/BPA_049810

Neben, A. R., Bradley, R. F., Hewitt, J. N., et al. 2016, ApJ, 826, 199

Ouchi, M., Shimasaku, K., Furusawa, H., et al. 2010, ApJ, 723, 869

Paciga, G., Chang, T.-C., Gupta, Y., et al. 2011, MNRAS, 413, 1174

Pacucci, F., Mesinger, A., Mineo, S., & Ferrara, A. 2014, MNRAS, 443, 678

Park, H., Shapiro, P. R., Komatsu, E., et al. 2013, ApJ, 769, 93

Parsons, A., Pober, J., McQuinn, M., Jacobs, D., & Aguirre, J. 2012a, ApJ, 753, 81

Parsons, A. R., Liu, A., Ali, Z. S., & Cheng, C. 2016, ApJ, 820, 51

Parsons, A. R., Pober, J. C., Aguirre, J. E., et al. 2012b, ApJ, 756, 165

Parsons, A. R., Backer, D. C., Foster, G. S., et al. 2010, AJ, 139, 1468

Parsons, A. R., Liu, A., Aguirre, J. E., et al. 2014, ApJ, 788, 106

Parsons, A., Backer, D., Chang, C., et al. 2006, in Asilomar Conf. on Signals and Systems (Pacific Grove, CA), 2031

Parsons, A., Backer, D., Siemion, A., et al. 2008, PASP, 120, 1207

Patra, N., Parsons, A. R., DeBoer, D. R., et al. 2017, arXiv:1701.03209

Pentericci, L., Vanzella, E., Fontana, A., et al. 2014, ApJ, 793, 113

Planck Collaboration, Ade, P. A. R., Aghanim, N., et al. 2015, arXiv:1502.01589

Pober, J. C., Parsons, A. R., Aguirre, J. E., et al. 2013a, ApJL, 768, L36

Pober, J. C., Parsons, A. R., DeBoer, D. R., et al. 2013b, AJ, 145, 65

Pober, J. C., Liu, A., Dillon, J. S., et al. 2014a, ApJ, 782, 66

Pober, J. C., Ali, Z. S., Parsons, A. R., et al. 2015, ApJ, 809, 62

Pober, J. C., Greig, B., & Mesinger, A. 2016a, MNRAS, 463, L56

Pober, J. C., Hazelton, B. J., Beardsley, A. P., et al. 2016b, ApJ, 819, 8

Pritchard, J. R., & Furlanetto, S. R. 2007, MNRAS, 376, 1680

Reich, W., Reich, P., & Fuerst, E. 1990, A&AS, 83, 539

Robertson, B. E., Ellis, R. S., Furlanetto, S. R., & Dunlop, J. S. 2015, ApJL, 802, L19

Rogers, A. E. E., & Bowman, J. D. 2012, RaSc, 47, RS0K06

Santos, M. G., Cooray, A., & Knox, L. 2005, ApJ, 625, 575

Schenker, M. A., Ellis, R. S., Konidaris, N. P., & Stark, D. P. 2014, ApJ, 795, 20

Schenker, M. A., Stark, D. P., Ellis, R. S., et al. 2012, ApJ, 744, 179

Schenker, M. A., Robertson, B. E., Ellis, R. S., et al. 2013, ApJ, 768, 196

Schroeder, J., Mesinger, A., & Haiman, Z. 2013, MNRAS, 428, 3058

Silva, M., Santos, M. G., Cooray, A., & Gong, Y. 2015, ApJ, 806, 209

Stevenson, M. & C-BASS Collaboration 2010, in Bulletin of the American Astronomical Society 42, American Astronomical Society Meeting Abstracts #215, 602

Sullivan, I. S., Morales, M. F., Hazelton, B. J., et al. 2012, ApJ, 759, 17

Tarter, J. C., Backus, P. R., Mancinelli, R. L., et al. 2007, AsBio, 7, 30

Tegmark, M. 1997, ApJL, 480, L87

Thompson, A. R., Moran, J. M., & Swenson, G. W., Jr. 2001, Interferometry and Synthesis in Radio Astronomy (2nd ed.; New York: Wiley-Interscience)

Thyagarajan, N., Parsons, A. R., DeBoer, D. R., et al. 2016, ApJ, 825, 9

Thyagarajan, N., Udaya Shankar, N., Subrahmanyan, R., et al. 2013, ApJ, 776, 6

Thyagarajan, N., Jacobs, D. C., Bowman, J. D., et al. 2015a, ApJL, 807, L28

Thyagarajan, N., Jacobs, D. C., Bowman, J. D., et al. 2015b, ApJ, 804, 14

Tingay, S. J., Goeke, R., Bowman, J. D., et al. 2013, PASA, 30, 7

Treu, T., Trenti, M., Stiavelli, M., Auger, M. W., & Bradley, L. D. 2012, ApJ, 747, 27

Trott, C. M., Pindor, B., Procopio, P., et al. 2016, ApJ, 818, 139

Tseliakhovich, D., Barkana, R., & Hirata, C. M. 2011, MNRAS, 418, 906

Tseliakhovich, D., & Hirata, C. 2010, PhRvD, 82, 083520

van Haarlem, M. P., Wise, M. W., Gunst, A. W., et al. 2013, A&A, 556, A2

Vedantham, H., Udaya Shankar, N., & Subrahmanyan, R. 2012, ApJ, 745, 176

Vrbanec, D., Ciardi, B., Jelić, V., et al. 2016, MNRAS, 457, 666

Welch, J., Backer, D., Blitz, L., et al. 2009, IEEEP, 97, 1438

Winglee, R. M., Dulk, G. A., & Bastian, T. S. 1986, ApJL, 309, 59

Yatawatta, S., de Bruyn, A. G., Brentjens, M. A., et al. 2013, A&A, 550, A136

Zackrisson, E., Inoue, A. K., & Jensen, H. 2013, ApJ, 777, 39

Zahn, O., Reichardt, C. L., Shaw, L., et al. 2012, ApJ, 756, 65

Zarka, P. 2011, Planetary Radio Emissions VII (Vienna: Austrian Academy of Sciences Press), 287

Zheng, H., Tegmark, M., Buza, V., et al. 2014, MNRAS, 445, 1084